ABSTRACT

Title of dissertation: PHOTOCATHODES: MAPPING,
CONTROLLED POROSITY,
CESIUM, AND GOLD

Blake C. Riddick, Doctor of Philosophy, 2013

Dissertation directed by: Professor Patrick G. O'Shea
Department of Physics

Photocathodes play a critical role in a large variety of applications, from detectors in medical imaging to electron beam sources for fundamental science. Via the photoelectric effect, photocathodes emit electrons in response to light of sufficient energy. Three important characteristics of photocathodes are quantum efficiency (the fraction of incident photons that generates emitted electrons), lifetime (how long the cathodes are operational), and emission uniformity. Coating a photocathode with an atomic layer of cesium dramatically improves quantum efficiency, but the inherent fragility of this layer worsens lifetime. The design and testing of a cesium rejuvenation system which prolongs lifetime will be presented, and a controlled porosity design which could improve emission uniformity will be discussed. A new method of mapping quantum efficiency will be presented. The initial results of testing cesium auride will be discussed, as they show the cathodes have surprisingly high quantum efficiency and the potential for very long lifetime.

PHOTOCATHODES: MAPPING, CONTROLLED POROSITY, CESIUM, AND GOLD

by

Blake C. Riddick

Dissertation submitted to the Faculty of the Graduate School of the
University of Maryland, College Park in partial fulfillment
of the requirements for the degree of
Doctor of Philosophy
2013

Advisory Committee:
Professor Patrick G. O'Shea, Chair/Advisor
Professor Theodore L. Einstein
Professor Rami Kishek
Professor Victor L. Granatstein
Professor Min Ouyang

Dedication

To the memory of my grandmothers Nana (Jane Cutler) and Baba (Nellie Riddick) and my great-aunts Hannah Windley and Lottie Romich.

Acknowledgments

conversations. Thanks to Drs. Theodore Einstein, Rami Kishek, Victor Granatstein, and Min Ouyang for serving on my dissertation committee. Dr. Einstein has given me great advice since I first met him in my freshman year as an undergrad, and inspired me to switch to physics from math. Dr. Ellen Williams was a wonderful advisor to me when I was an undergrad and a beginning graduate student. Thanks to Dr. Roberto Maass-Moreno for being a terrific mentor, neighbor, and friend.

Thank you to all my family and friends for supporting me over the years. Thanks to Lyndell Wehab and everyone in Belhaven for always making me feel at home. Thanks to my parents, Drs. Howard and Carol Riddick for all their love and support. Thanks to my brother Ryan Riddick for being my closest friend. Finally, thanks to my wife Haiwen Ding for these past 4 years of happiness, and many more to come.

Table of Contents

List of Tables

List of Figures

List of Abbreviations

CCR	Calabazas Creek Research
CCD	Charge-Coupled Device
CPD	Controlled Porosity Dispenser
DMD	Digital Micromirror Device
IREAP	Institute for Research in Electronics and Applied Physics
MFP	Mean Free Path
PEEM	Photoemission Electron Micropscopy
QE	Quantum Efficiency
UMD	University of Maryland

Chapter 1: Introduction

In the search for intense and long-lifetime sources of electron beams, photocathodes are promising, but still fall short. Photocathodes, materials with favorable photoelectric emission, already play a critical role in large variety of applications, from being used as detectors in medical imaging to being electron sources for fundamental physics experiments.

Einstein won the Nobel Prize for his theory of the photoelectric effect in 1921, but by no means was the understanding of photoemission complete at this point. Explaining why some materials are much better photocathodes than others is to this day an active area of research, and is crucial to moving from the historical approach to photocathode design of mostly trial, error, and luck [1] to one based on fundamental physical principles.

Three important characteristics of photocathodes are quantum efficiency (the fraction of incident photons that generates emitted electrons), lifetime, and emission uniformity. Higher quantum efficiency allows more charge to be extracted for a given drive laser, or conversely it allows the same amount of charge to be extracted with a lower power laser. Photocathodes have limited lifetime due to changing conditions on the surface. Increasing photocathode lifetime allows for greater up-time

in experiments, so there is a strong emphasis on research on this aspect. Emission uniformity is important when the quality of the electron beam matters.

In this dissertation we will discuss our research on making more efficient photocathodes. We have developed a new cathode design which dramatically increases lifetime while maintaining emission uniformity. And we have pioneered a quantum efficiency mapping technique which allows us to directly measure emission uniformity.

1.1   The Photoelectric Effect

To provide context for these advances, we will begin with the photoelectric effect. First observed by Hertz in 1887, the photoelectric effect challenged the predominant wave theory of light [2]. In addressing this issue, Einstein developed a quantum theory of light, wherein light can exhibit particle-like properties in cases such as the photoelectric effect. This, along with de Broglie's suggestion that particles can exhibit wave-like properties (later verified experimentally), led to the wave-particle duality central to quantum mechanics [3]. Einstein's theory of the photoelectric effect follows directly from the idea of quantized light and explains the elementary aspects of photoemission.

The theory depends on two parameters: one from the incident light, and one from the cathode. Each particle of light (photon) has an energy $h\nu$, where h is Planck's constant, and ν is the light's frequency. Some electrons in the cathode will absorb one photon, increasing their kinetic energies. If a photo-excited electron has

sufficient energy, it can escape from the cathode. The cutoff energy, below which there is no photoemission, is dependent on the cathode, and is called the work function, Φ_w. So the upper limit on the kinetic energy of the electrons that escape is:

$$K = h\nu - \Phi_w \tag{1.1}$$

As the key players in the photoelectric effect, photons and electrons set the energy, time, and length scales. Planck's constant is 4.136 eV·fs, where 1 eV is the amount of energy an electron gains after moving across a potential difference of 1 volt (1 eV = 1.602 $\times 10^{-19}$ J) [4]. UV, visible, and IR lasers are the typical light sources, with wavelengths between 200 and 1000 nm. With the relation $c = \lambda\nu$, with λ the wavelength and c the speed of light in vacuum, this wavelength range corresponds to frequencies of between 300 and 1500 THz (periods around 1 fs), and energies of between 1 and 6 eV. Work functions of bare metals are typically between 3 and 5 eV. A useful relation to get energy E from wavelength λ is

$$E[\text{eV}] \approx \frac{1240}{\lambda[\text{nm}]} \tag{1.2}$$

with numerical values for the units indicated. For example, $\lambda = 532 \; nm$ would return 2.33 eV.

Einstein's theory explained the challenges to the classical theory of the photoelectric effect, but it is not complete since work functions are determined experimentally. Additionally, even with light of sufficient energy to overcome the work function, not every incident photon results in an emitted electron. The ratio of the number of emitted electrons to incident photons is called quantum efficiency (QE),

and its value depends on the cathode material. There has been vast improvement in electron emission theory [5], but understanding QE from basic physical principles is still a fundamental goal of photocathode research.

1.2 Quantum Efficiency, Lifetime, Response Time, and Materials

One can experimentally determine QE from measured photocurrent I and laser power P:

$$\text{QE} = \frac{\#\text{ electrons out}}{\#\text{ photons in}} = \frac{hc}{\lambda}\frac{I}{P} \approx \frac{1240}{\lambda[\text{nm}]}\frac{I[\text{A}]}{P[\text{W}]} \tag{1.3}$$

since

$$I = (\#\text{ electrons out})e/(\text{unit time}) \tag{1.4}$$

$$P = (\#\text{ photons in})(\text{photon energy}/\text{unit time}) \tag{1.5}$$

with e being the electric charge, λ the laser wavelength, photon energy is hc/λ, and $hc \approx 1240$ eV·nm. The last expression in Eq. (1.3) returns the value of QE, which is unitless, when the numerical values for the parameters are input for the units indicated (e.g., a wavelength of 532 nm would be input as 532). QE is reported as either a fraction of 1 or a percentage. For bare metals, QE is typically on the order of 0.01%.Photocathodes made of specially coated semiconductors can have QEs on the order of 10%, but are often short-lived, whereas bare metals are long-lasting [6].

The low QE of metals (and the higher QE of semiconductors) is well explained with Spicer's three-step model [7], which can be seen in Figs. 1.1 and 1.2. The first step is optical absorption. Many electrons are reflected from the surface of a metal (up to near 40%). Reflectivity causes a dramatic decrease in QE as defined here. One

must be careful when comparing commercially manufactured photocathode data, as they will sometimes remove this reflectivity from their definition of QE, resulting in a misleadingly higher number. Photons that are not reflected are absorbed at some depth from the cathode surface, characterized by a penetration depth and exponential decay. The penetration depth is on the order of the light's wavelength.

In the second step, electron transport, the electrons that absorb a photon travel in a random direction. So roughly half will be going in wrong directions, away from the surface. In metals, there are many free electrons, so there is a very high probability that a photoelectron will scatter off one or more. How much energy the photoelectron loses depends on how direct the collision is, with glancing collisions causing a smaller energy decrease. In most instances, neither the scattered photoelectron nor the secondarily excited electron will have sufficient energy to escape from the cathode. For semiconductors, electron-phonon scattering is dominant, resulting in a relatively negligible decrease in electron energy; this is where semiconductors' high QE comes from. This higher QE comes at a cost. Since the electrons can scatter many times, some will take convoluted paths to the surface. So whereas metals have response times to incident light on the order of femtoseconds, semiconductors can have emission tails in time going up to nanoseconds. In RF cavities, which typically operate at around 1 GHz (period scale 1 ns), the emission tails can be problematic when those delayed photoelectrons encounter suboptimal accelerating gradients.

In the final step, escape across the surface, the electrons need sufficient energy to overcome the energy barrier between the cathode and vacuum. Electrons with
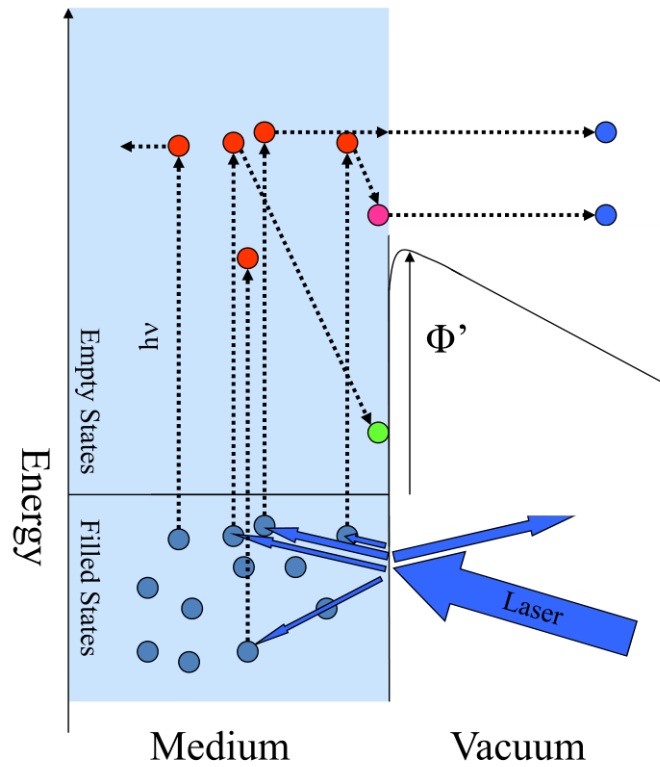
Figure 1.1: Photoemission in metals. Some light is reflected from the surface. Electron-electron scattering is dominant, reducing most photoexcited electrons to below the effective work function Φ', which is reduced from the work function due to the applied field (Schottky effect). Image from J. Smedley [8].
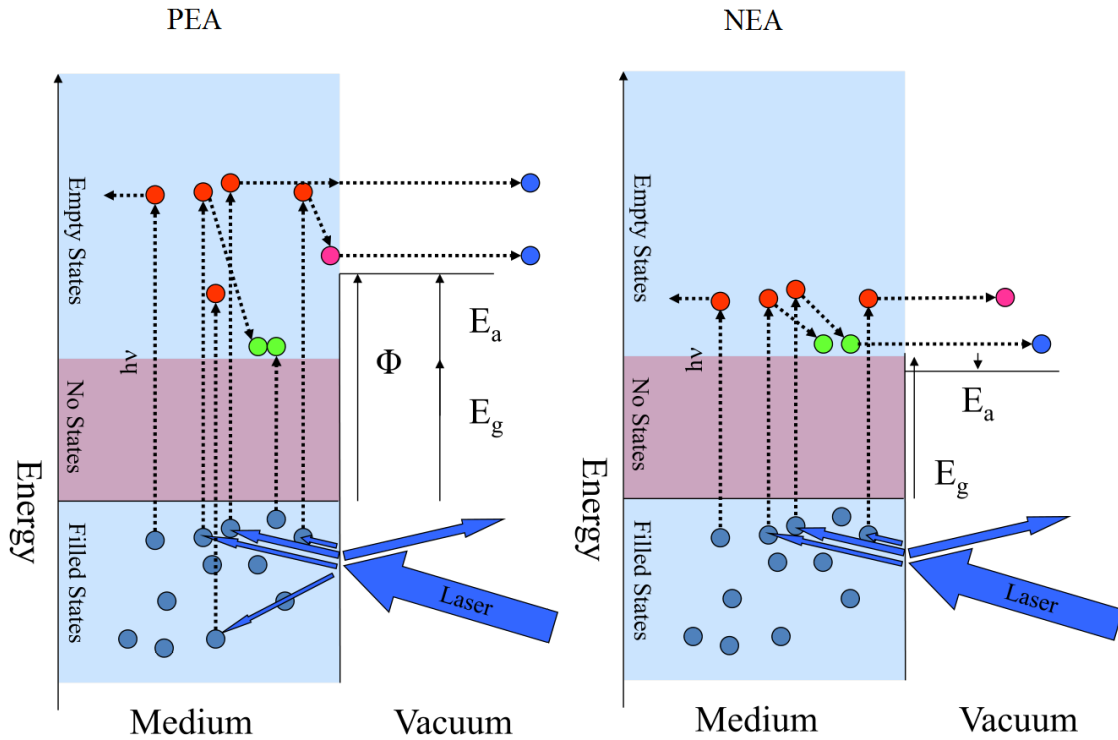
Figure 1.2: Photoemission in positive electron affinity (PEA) and negative electron affinity (NEA) semiconductors. Some light is reflected from the surface. Electron-phonon scattering is dominant, so more photoexcited electrons can reach the surface with energy either above the band gap E_g plus the electron affinity E_a for PEA semiconductors, or for any energy in the conduction band for NEA semiconductors. Image from J. Smedley [8].

less energy than the work function can escape due to the Schottky effect of effective work function lowering and quantum tunneling through the potential barrier. In the modified Fowler-Dubridge model for metals developed by Jensen [5], one can see the three steps:

$$QE \propto [1 - R(\lambda)]F(\lambda, \delta, \tau) \left(\frac{hc}{\lambda} - \Phi'_w \right)^2 \tag{1.6}$$

with reflectivity R, a scattering factor F dependent on penetration depth δ and scattering rate (relaxation times) τ, and a quadratic dependence on the difference between photon energy $\frac{hc}{\lambda}$ and the effective work function Φ'_w. Note that QE is wavelength (λ) dependent.

Semiconductors can be split into those with positive electron affinity (PEA) and those with negative electron affinity (NEA). NEA cathodes can have the very long emission tails discussed previously, since any electron in the conduction band that makes its way to the surface can escape, no matter how many collisions it suffered nor how convoluted a path it took.

1.3   Photocathode Materials and the Importance of Cesium

The details of electron emission depend greatly on the choice of cathode material. A plot of QE versus lifetime can be seen in Fig. 1.3. We see that cesium based cathodes have a higher QE, but a lower lifetime. A sub-monolayer coating of cesium can reduce the work function of many materials, such as tungsten as shown in work from UMD in Fig. 1.4. Cesium is the most electropositive, naturally-occurring element. As can be seen from its position on the periodic table, it has one valence

electron which is greatly shielded from the nucleus by filled electron shells. With this loosely held electron, a cesium atom can form a dipole on the cathode surface which acts to effectively lower the local work function (within a few atomic radii). Other alkalis show this effect to a lesser extent since their valence electrons are not as well shielded and thus form weaker dipoles [5].

Depositing increasing amounts of cesium will continue to lower the local work functions up to a point where cesium atoms are packed close enough to interfere with neighboring dipole moments. The optimum coverage is typically between 50 and 60% of a monolayer. This behavior is well described by the modified Gyftopoulos-Levine theory developed by Jensen [5].

The reduced lifetime of cesium-based photocathodes is due to the inherent fragility of the submonolayer coverage of cesium. Contaminants in the vacuum system can quickly deplete the cesium layer. As a rule of thumb, at a pressure of 10^{-6} Torr due to a single element, a surface in vacuum will be exposed to a monolayer of that element every second. At 10^{-7} Torr, this would be every 10 s. Not every element or molecule will stick to a cathode surface, but this is still a useful guideline for considering contaminants. The lifetimes in Fig. 1.3 have been normalized to 1 nTorr using this rule of thumb. There are other factors which reduce lifetime, namely ion back-bombardment, wherein positive ions are accelerated into the cathode surface by the same fields which accelerate electrons away[*].

---

[*]Subsections 1.1-1.3 are taken, with minor modification, from the author's unpublished paper submitted for his M.S. and advancement to candidacy.

9
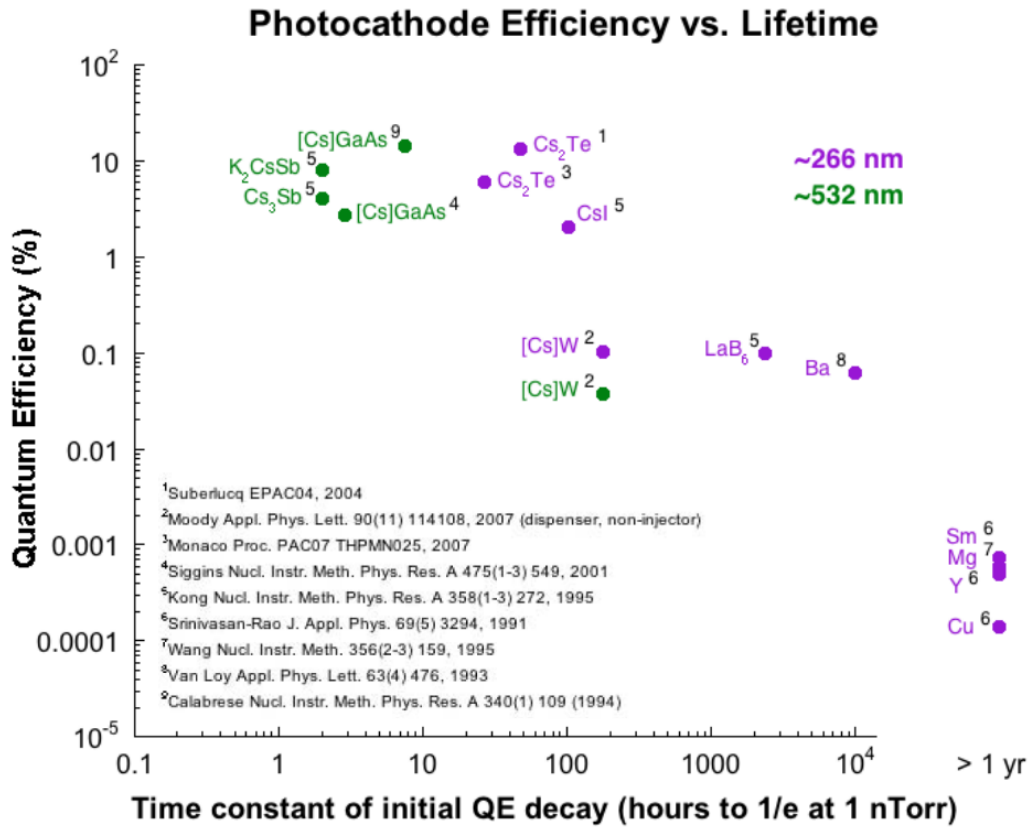
Figure 1.3: Quantum efficiency vs. lifetime for several photocathodes. Lifetimes have been normalized to 1 nTorr. Other lifetime-reducing effects are not not normalized, because contamination is presumed dominant [9].
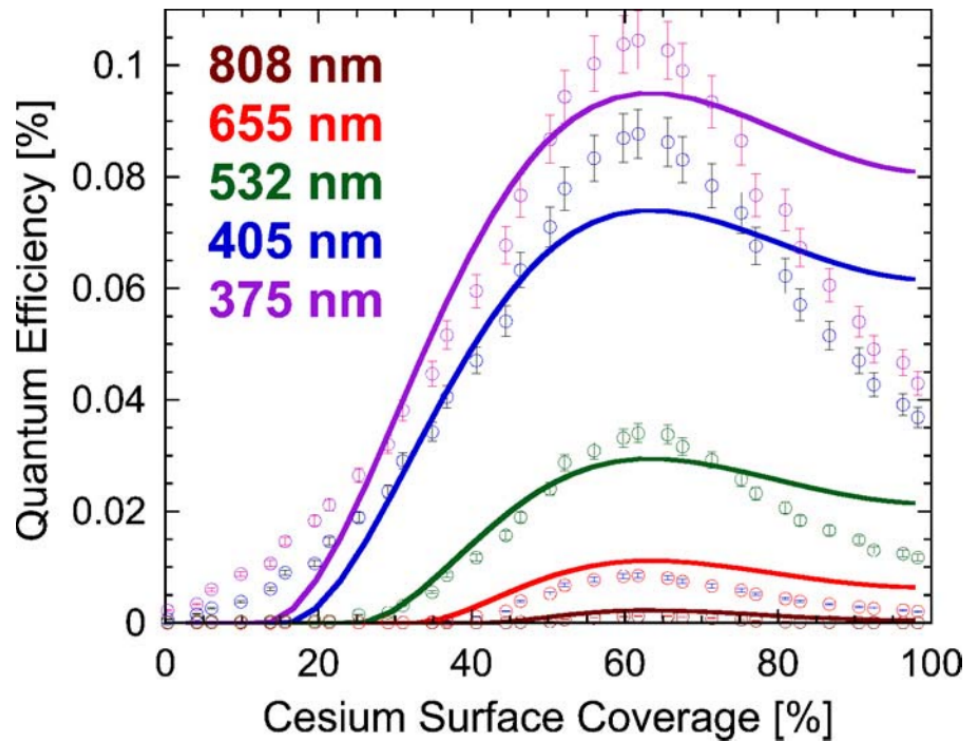
Figure 1.4: Quantum efficiency vs. cesium coverage on tungsten for several wavelengths. The experimental data are points and the lines are theory. 100% coverage corresponds to 1 monolayer. The QE is highest for the highest photon energy 375 nm light, and is successively lower for the longer wavelength lights [10].

1.4 Electron Beam Quality Parameters

1.4.1 Emittance

A key figure of merit for discussing the quality of an electron beam is emittance. Emittance is a measure of the compactness of the position-momentum phase space $\{x, y, z, p_x, p_y, p_z\}$ occupied by the electrons in a beam [11], and can be split into its transverse and longitudinal components. A beam is defined as a collection of particles with one velocity component much larger than the other two. If we say the electron beam is traveling in the z direction, then the total momentum of an electron is $p \sim p_z$. Focusing on the transverse directions x and y (see [12] for the longitudinal direction), we can then define a trace space $\{x, y, x', y'\}$ where

$$p_x, p_y \ll p_z \tag{1.7}$$

$$x' = \frac{dx}{dz} \approx \frac{p_x}{p_z} \approx \frac{p_x}{p} \tag{1.8}$$

and similarly for y'. Note that phase space and trace space are sometimes used interchangeably in the literature.

There are several definitions of emittance, so we will define precisely what we mean by emittance here. Namely, we take effective emittance in x to be

$$\epsilon_x = 4\sqrt{\langle x^2 \rangle \langle x'^2 \rangle - \langle xx' \rangle^2} \tag{1.9}$$

and similarly for y, with units of mm-mradians. The factor of 4 and further discussion of emittance are in Appendix A. To compare beams of different energies, it is necessary to normalize these emittances by multiplying by $\beta\gamma$, where $\beta = v/c$, v is

the speed of the electrons, c is the speed of light in vacuum, and $\gamma = [1 - \beta^2]^{-1/2}$.

An ideal electron beam would have all the electrons moving with the same velocity, as shown in Fig. 1.5, which would correspond to an emittance of 0. Real beams have emittances greater than 0 which are at best on the order of 1 mm-mrad. Nonlinear forces on the beam will increase emittance over time, so the intrinsic emittance at the cathode limits the final quality of the beam.

1.4.2 Brightness

Increased brightness is a key advantage photocathodes have over thermionic cathodes, which use heat to drive off electrons. Brightness is defined as

$$B = \frac{2I}{\pi^2 \epsilon_x \epsilon_y} \tag{1.10}$$

where I is the electric current. Photocathodes can have brightnesses 3 orders of magnitude greater than those of thermionic cathodes. As with emittances, normalized brightness (to compare beams of different energies) uses normalized emittances. From the definition of brightness, we see that increases in emittance cause decreases in brightness. Brightness is a measure of how dense a beam is; emittance is a measure of how well collimated and compact a beam is.

1.5 Outline

In the rest of this dissertation, we will discuss photocathode materials, fabrication, and testing. Chapter 2 will discuss the fabrication and testing of cesium auride. In chapter 3 we will detail a novel technique for making maps of quantum

efficiency. Chapter 4 is about a new photocathode design made in collaboration with Calabazas Creek Research which has been shown to have long lifetime and an incredible degree of robustness. Conclusions and plans for future work will be presented in Chapter 5.
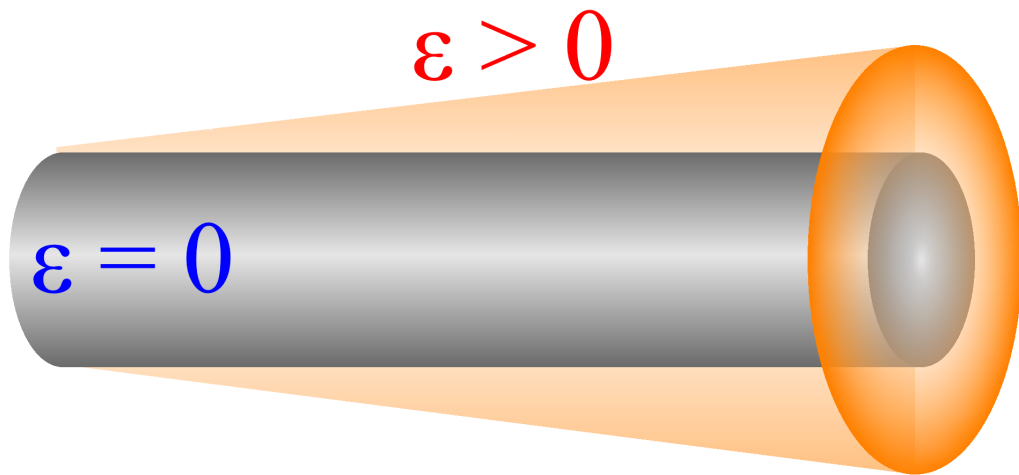
Figure 1.5: An idealized beam (configuration space shown) would have an emittance of 0. Real beams have transverse distributions which vary over time and have emittances greater than 0. Image from Kevin L. Jensen [13].

Chapter 2: A Hybrid-Diffuser, Controlled Porosity Dispenser Photo-cathode

2.1 Introduction

For many metals and semiconductors, a submonolayer cesium coating lowers the effective energy barrier to vacuum, thus allowing electrons to escape more readily. However, this coating tends to be very short-lived, which limits its usefulness. A cesium rejuvenation system has previously been shown to work with sintered tungsten powder photocathodes [14], prolonging the lifetime of improved electron emission by replenishing the cesium coverage as needed. While the cesium rejuvenation system is promising, before it can be tested in a system which requires an electron source, the rate at which cesium leaves the cathode needs to be determined. If this rate is too high, then one needs to worry about cesium contamination of other parts of the system, like an RF cavity. Ideally, the cesium flow rate would be just enough to replenish the cathode surface.

Traditional sintered tungsten cathodes are made with tungsten powder, and their density can be controlled by adjusting the powder grain size. However, there is no fine control over how the powder sinters together. As such, two cathodes with

the same density can have significantly different porosity and thus different cesium flow rates. This random porosity can also lead to non-uniform coverage of cesium on the cathode surface, which leads to non-uniform electron emission.

To address this issue of non-uniform cesium coverage, several methods have been developed to make controlled porosity dispenser (CPD) photocathodes, but these have been impractical for wide use. A new method [15], based on research from over 50 years ago, is very promising. Tungsten wires are sintered together, and then a cross section of these wires is taken to be used as the cathode. As can be seen in Fig. 2.1, these cathodes have a uniform pore distribution, and the pores have the same shape and size.

Predicting the cesium flow rate through a single pore is enough to predict the rate through the whole cathode. Deriving a scaling law for the cesium flow rate's dependence on cathode diameter, individual tungsten wire diameter, length, and temperature revealed that temperature is the dominant factor, and that the flow rate would be orders of magnitude greater than the flow rates of sintered tungsten powder cathodes.

After these calculations, we decided to construct the hybrid-diffuser cathode assembly seen in Fig. 2.2. The cesium reservoir is capped with a sintered tungsten powder cathode, followed by a small mixing region, and then finally a sintered tungsten wire cathode. We wanted the powder cathode to limit the cesium flow rate, while the wire cathode distributed cesium uniformly across the surface.

We tested this design using a prototype built by Calabazas Creek Research, and the results were very encouraging. We were able to cesiate the cathode sur-
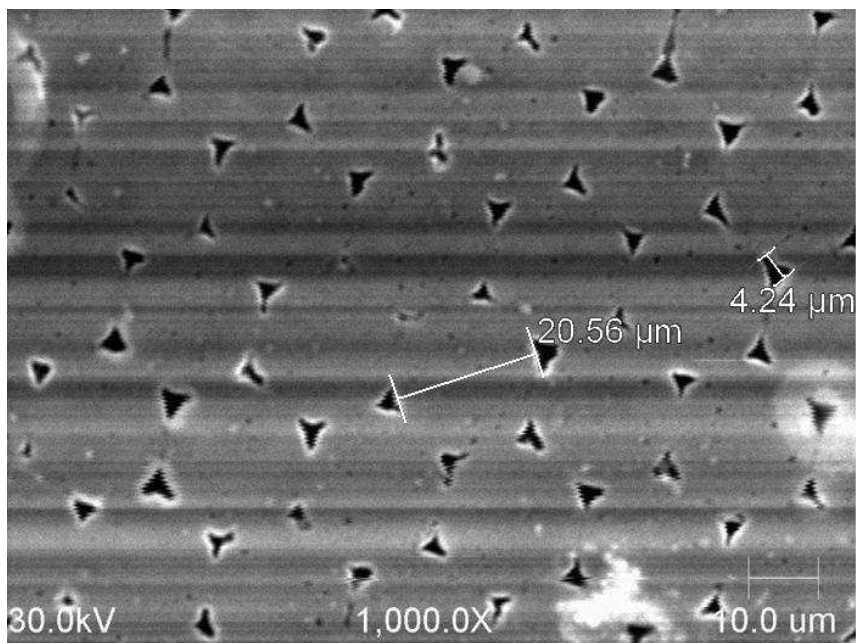
Figure 2.1: Controlled porosity dispenser photocathode [15].

Sintered Powder Diffuser

Heater Sleeve

Cesium Reservoir

CPR Emitter

Mixing Region
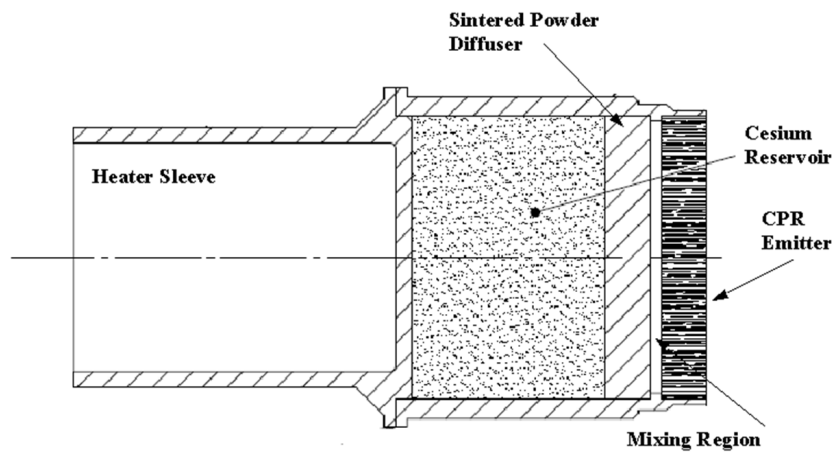
Figure 2.2: Hybrid-diffuser controlled porosity dispenser photocathode [16].

face, and replenish the surface as needed after many partial leaks to atmospheric contamination. The cesium evaporation rate from the surface was three orders of magnitude less during cesium rejuvenation than the rate when just using a sintered powder cathode. Lifetime is estimated to be 30,000 hours.

After performing all our planned experiments, we took the already activated cathode out of the vacuum chamber, and let it sit in air for 9 hours as we worked on the QE test stand. We reinstalled the cathode and followed standard vacuum bakeout procedures. When we heated the cathode, we saw photoemission again.

In this chapter, we will discuss the models used to design this long-lifetime, hybrid-diffuser cathode with a cesium reservoir. We will then detail the experiments we performed. The novel technique to determine the uniformity of electron emission will be discussed in the following chapter.

2.2   Designing and Modeling the Controlled Porosity Photocathode

2.2.1   Knudsen Number

Standard Knudsen theory (created in 1909, for a review, see [17]) can model the flow rate of cesium through thin pores. Specifically, this theory is only valid if the mean free path (MFP) λ_{MFP} of the cesium is much larger than the cross-sectional pore size R; that is, the Knudsen number,

$$K_n = \frac{\lambda_{\mathrm{MFP}}}{R} \tag{2.1}$$

needs to be much larger than unity [17]. Since the Knudsen number will only be used to ensure that the theory is applicable, an order-of-magnitude estimation is sufficient. If the cesium is assumed to be an ideal gas, then the mean free path can be written [18] as

$$\lambda_{\mathrm{MFP}} = \frac{k_B T}{\pi \sqrt{2} d^2 p} \approx 2 \text{ km} \tag{2.2}$$

with Boltzmann constant $k_B \approx 10^{-23}$ J/K, temperature $T \approx 10^3$ K, cesium hard shell diameter $d \approx 1$ nm, and background pressure $p \approx 10^{-8}$ Torr $\approx 10^{-6}$ Pa. The mean free path is much larger than the pore size of about 4 microns, so Knudsen theory can be applied.

2.2.2   Derivation

The mass flow rate Q, through a pore of cross sectional area A, with atoms of mass M being absorbed and re-emitted from the interior surface (or wall) of the tubes S, can be given as a function of the differential surface area dS, the differential cone spherical angle $d\Omega$, the flux $F(z)$ into the wall S a distance z from the end of the tube, and the distribution in angle from the normal, $f(\theta)$. These parameters can be seen in Fig. 2.3, for a cylindrical pore.

Determining the mass flow rate entails a series of integrals [19]. Before getting to the results, the key assumptions of the model should be emphasized. With such a long MFP, the cesium atoms are assumed to not interact with each other nor collide. They travel in straight lines until they hit the wall, where they are reflected diffusively. So the reflection follows a cosine law from the normal to the wall. Also,
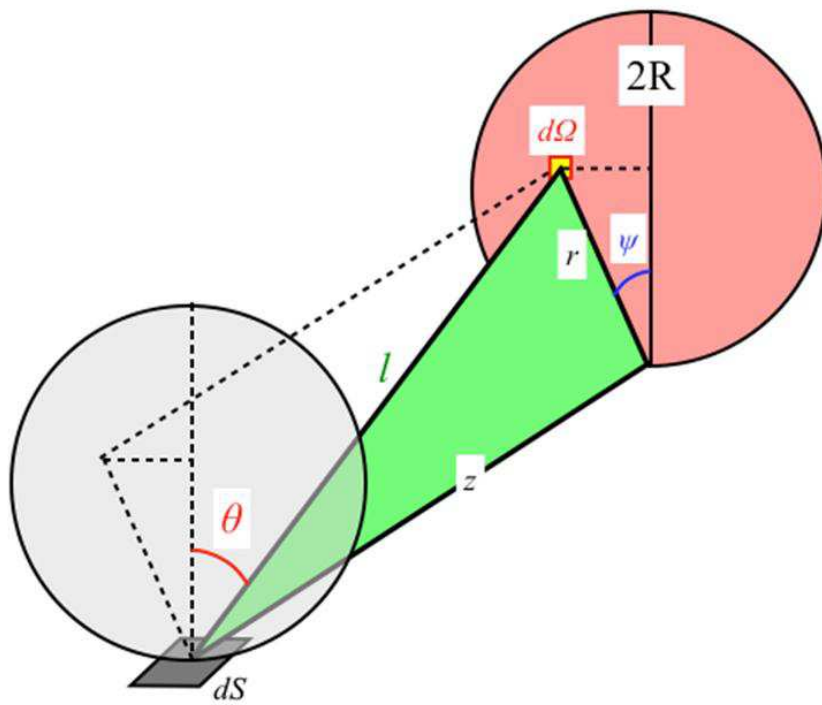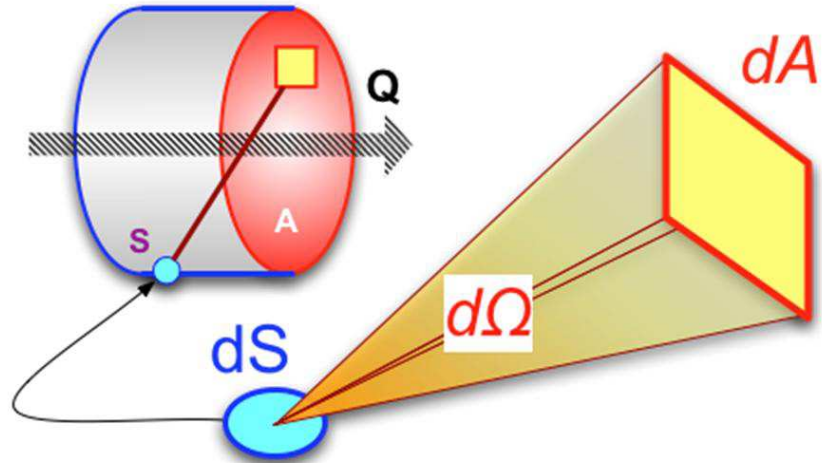
Figure 2.3: Identification of parameters used to determine the mass flow rate for a cylindrical pore. (Courtesy of K.L. Jensen [13])

the cesium atoms are approximated by a Maxwellian distribution of velocity.

With this in mind, the integrals can be set up to find the mass flow rate:

$$Q_{\text{pore}} = M \int dS \int d\Omega \, F(z) f(\theta) \tag{2.3}$$

After calculation, this becomes

$$Q_{\text{pore}} = \langle \cos \psi \rangle_A \frac{A P_A}{2L} \left(\frac{M}{2\pi k_B T} \right)^{1/2} p(T) \tag{2.4}$$

where P_A is the perimeter of the pore. $p(T)$ is the cesium pressure as a function of temperature, and will be discussed later. From this equation for Q_{pore}, useful scaling laws can be derived.

2.2.3   Scaling Laws

If pore area is kept constant, then the only two other spatial factors are perimeter and $\langle \cos \psi \rangle_A$. Table 2.1 shows the independently calculated values for circular, triangular, and square pores keeping area constant. To be noted is that triangles and squares are not rotationally symmetric, so the integration across ψ depends on their orientation. The integrals could be averaged over all orientations, but it is easier to use two extreme cases and average them. A triangle pointing up and one pointing down were used, as were a square as shown and one rotated 45°. As can be seen in Table 2.1, the numbers do not change very much, which is to our knowledge a new result. So for many situations it would be acceptable to use a circular pore for calculations. In the case of these CPD cathodes, the pores are very well approximated by triangles for more precise calculations.

23

	◯	△	☐
$\langle \cos \psi \rangle_A$	0.849	0.836	0.853
P_A	1	1.29	1.13

Table 2.1: $\langle \cos \psi \rangle_A$ and perimeter P_A for different pore shapes of equal area.

If R is taken to be the characteristic size, e.g., the radius, of the pore, then $A \sim R^2$ and $P_A \sim R$. For a given temperature, this leaves:

$$Q_{\text{pore}} \sim \frac{R^3}{L} \tag{2.5}$$

However, this is not the whole story. For an entire cathode with N pores, the total mass flow rate is

$$Q = NQ_{\text{pore}} \tag{2.6}$$

For a CPD cathode of diameter D_c made with individual wires of diameter D_w, the number of pores goes like $N \sim D_c^2/D_w^2$. If it is assumed that D_w scales linearly with R then this leaves

$$Q \sim \frac{D_c^2 D_w}{L} \tag{2.7}$$

It is important to separate the cathode area from the pore size. The incident laser light needs to be focused on the cathode, and if the cathode is small enough, the intensity can thermally damage the cathode. For cathodes made with smaller pores, the flow through each pore is greatly reduced, but for a fixed cathode area, there are more pores. If the cathode area is taken to be independent from pore size, then the strong R^3 dependence is lost. What is left is the simple scaling law (2.7) for spatial factors.

To determine the temperature dependence of Q, the pressure of cesium inside the reservoir is needed. This is approximated to be the vapor pressure of cesium, which has been measured, and is

$$p(T) = p_0 e^{-T_0/T} \tag{2.8}$$

with empirically determined constants $p_0 = 1.11 \times 10^7$ Torr and $T_0 = 8820$ K (corresponding to an energy of 0.751 eV) [20]. So for a given cathode,

$$Q \sim \frac{1}{\sqrt{T}} e^{-T_0/T} \tag{2.9}$$

Together, this gives a total scaling law

$$Q \sim \frac{D_c^2 D_w}{L} \frac{1}{\sqrt{T}} e^{-T_0/T} \tag{2.10}$$

Finally, one can estimate how long a cesium dispenser would last by dividing the total cesium mass M_{tot} by the mass flow rate Q:

$$\tau \sim M_{\text{tot}} \frac{L}{D_c^2 D_w} \sqrt{T} e^{T_0/T} \tag{2.11}$$

2.2.4   Calculations and Predictions

While scaling laws are useful for determining how parameters affect a system, it is also important to get an idea for the quantitative scales involved. To do this, the pores are approximated as triangular with height (not side) $h = 4.24$ μm and the individual wire diameter is taken to be $D_w = 20.56$ μm, as seen in Figure 2.1. An approximation will more readily allow the comparison of different cathodes, and make the dependencies of the mass flow rate clearer. This is the same approximation used to get to (2.7), which is to assume that $D_w = Sh$, with $S = 4.85$ being a scaling factor that is constant as D_w and h change. With this it can be seen that for one pore, $Q_{\text{pore}} \sim h^3$, but for the whole cathode, $Q \sim h$. This is because for a given cathode area, if D_w is increased, the number of pores decreases, while the flow through a single pore increases, thus reducing the strong h^3 dependence to only an h dependence.

With this approximation, the mass flow rate is

$$Q = \frac{\pi}{S^3\sqrt{3}} \frac{D_c^2 D_w}{L} \left(\frac{M}{2\pi k_b T} \right)^{1/2} p_0 e^{-T_0/T} \tag{2.12}$$

From this expression, one can see the dependence on the wire diameter D_w and the temperature T. Using a cathode of area of 1 cm^2, $L = 1$ mm, and a cesium reservoir with $M_{\text{tot}} = 10$ mg gives the results shown in Figures 2.4 and 2.5*.

2.2.5 The Hybrid-Diffuser Design

As we can see from Fig. 2.5, for temperatures around 550 K (the activation temperature for the Cs-Bi compound), the mass flow rate is near $10^5 \, \mu$g/cm^2/hr. This is far too high, since this means about 10^6 monolayers of cesium per hour are contaminating the vacuum system.

So we choose to use the hybrid dispenser design shown in Fig. 2.2. The sintered tungsten powder cathode placed between the wire cathode and the cesium reservoir had previously been shown to have a cesium mass flow rate of less than $1 \, \mu$g/cm^2/hr [21]. We wanted to use the powder cathode to limit the flow rate of cesium, and the wire cathode to distribute the cesium uniformly across the illuminated surface.

---

*Subsections 2.2.1-2.2.4 are taken from the author's unpublished paper submitted for his M.S. and advancement to candidacy.
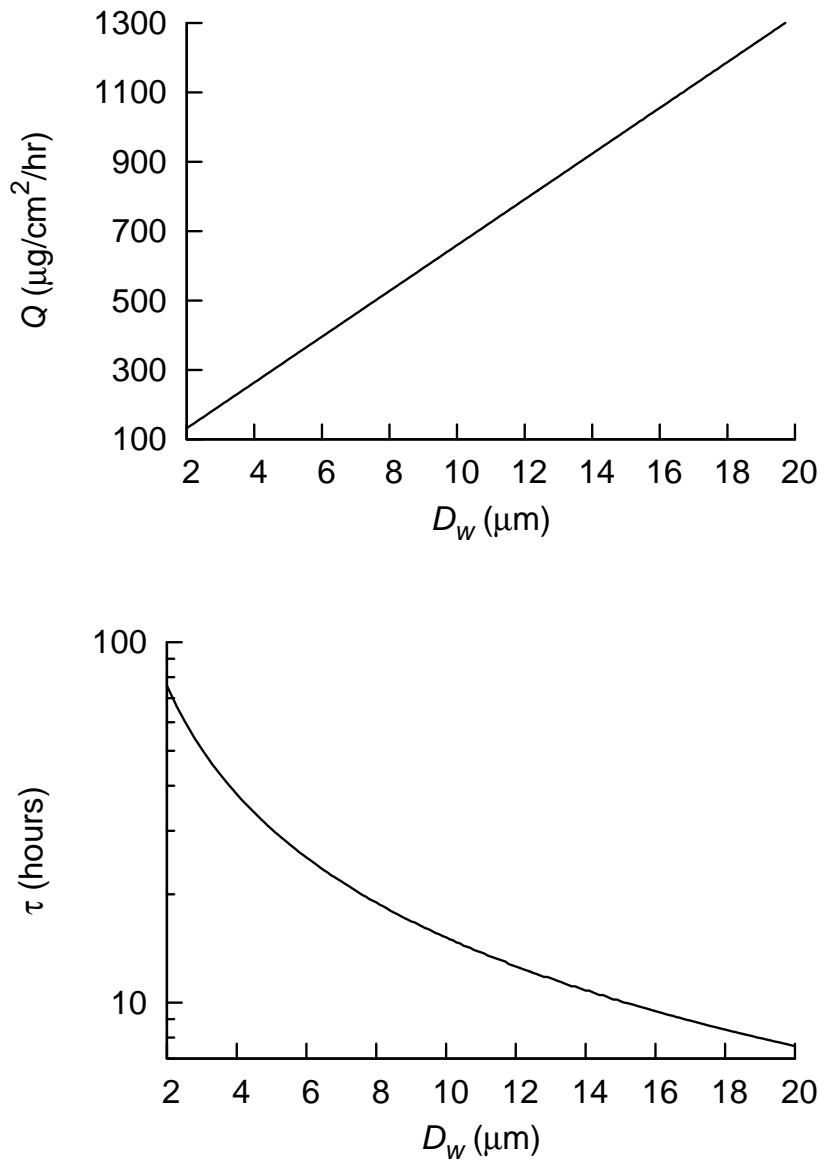
Figure 2.4: Mass flow rate Q and lifetime τ as a function of individual tungsten wire diameter D_w with temperature fixed at 450 K.
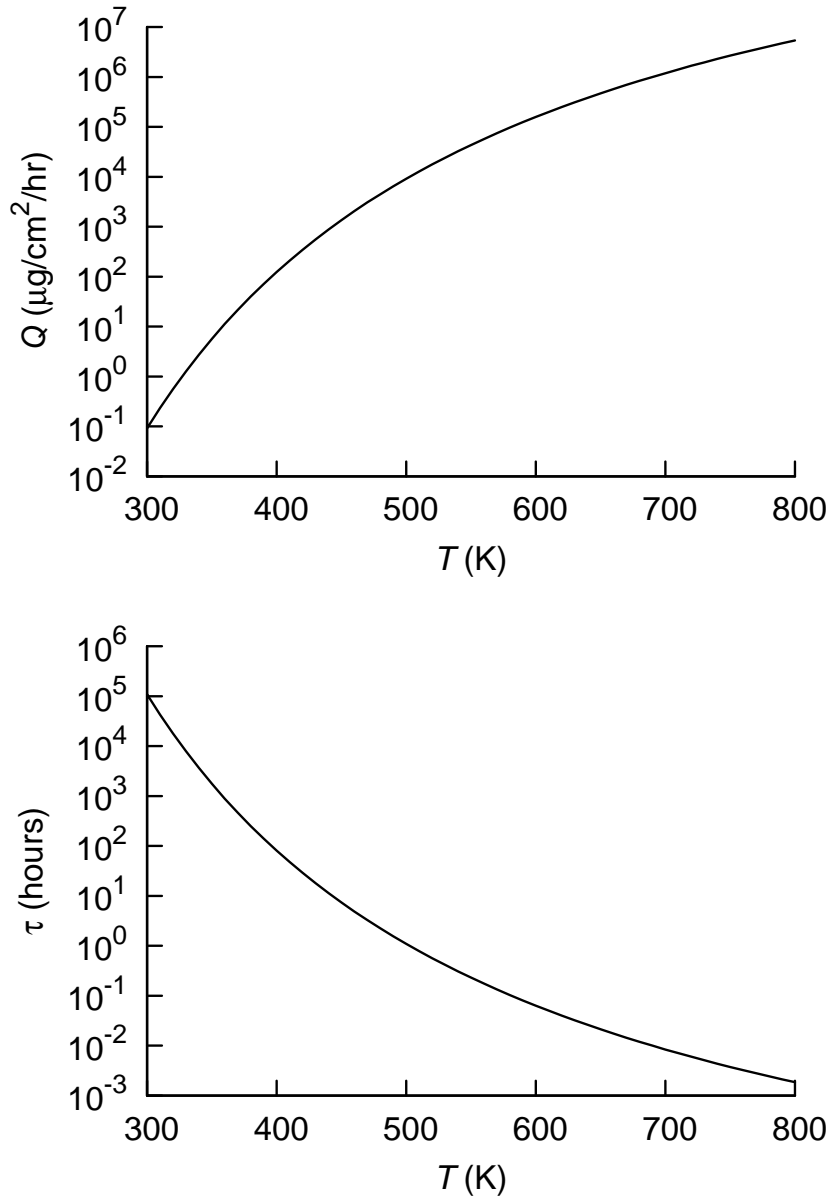
Figure 2.5: Mass flow rate Q and lifetime τ as a function of temperature T with individual tungsten wire diameter D_w fixed at 20.56 μm.

2.3 Experimental Results

2.3.1 Temperature Cycling

After installing the cathode in our test chamber and following our usual bake-out procedures, we heated the cathode to over 500°C for two days, after which we began to see photoemission due to cesium finally reaching the cathode surface. This time between initial heating and photoemission is consistent with previous tests with just a sintered powder cathode [22], where the activation time was around 20 hours. It takes this long for the cesium to diffuse through the bulk of the cathode.

After this initial activation, the cathode responded quickly to changes in temperature. At room temperature, the vacuum pressure was 5×10^{-10} Torr. Figure 2.6 shows the QE response of the cathode to thermal cycling at different temperatures. At 150°C, there is a double peak for each cycle of temperature. The first peak is due to over-cesiation of the cathode surface. When the cathode heater is turned off, the cesium is evaporating from the cooling, but still hot, surface. The evaporation continues with the cesium coverage dropping below the optimum value, and so the QE goes through a second peak [23].

When the temperature was increased to 325°C, the double peaks are more pronounced. When the temperature was lowered to 125°C, we see the double peaks disappear, as we have found the equilibrium point between cesium supply from the reservoir and evaporation of cesium from the cathode surface.
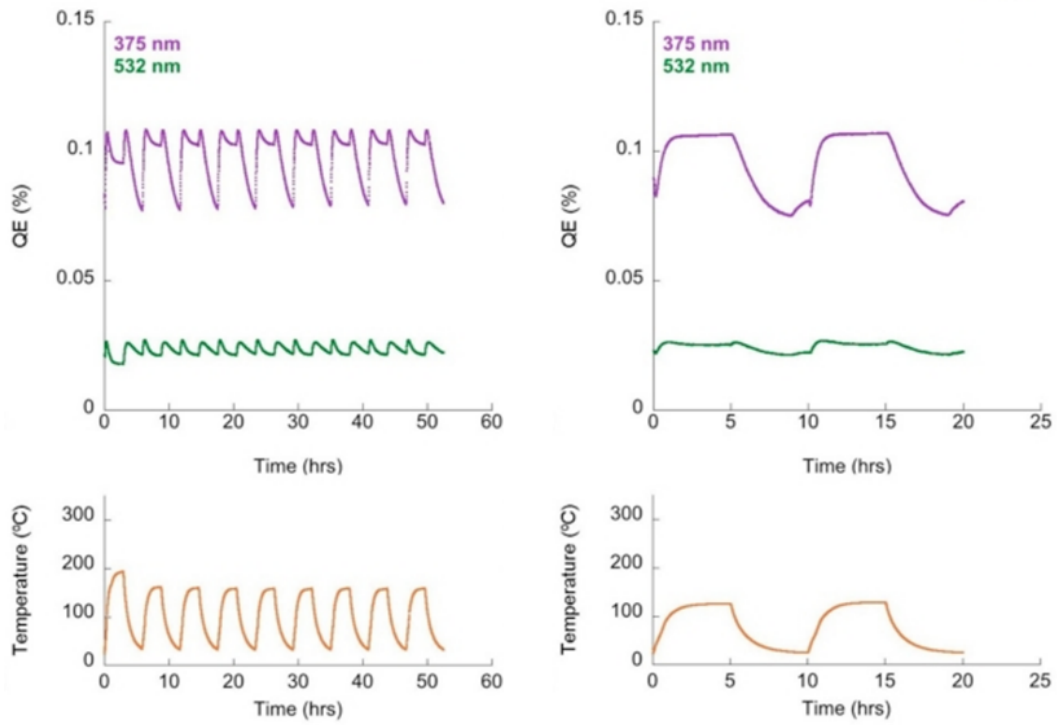
Figure 2.6: Thermal cycling of the hybrid dispenser cathode to 150°C (left column), and 125°C (right column). For the top row, the QE is higher for the higher photon energy 375 nm light when compared to that of the 532 nm light [23].

2.3.2 Cesium Mass Flow Rates And Estimated Lifetimes

During the temperature tests, we had a quartz crystal microbalance (QCM) facing the cathode to monitor the amount of cesium leaving the surface. In Fig. 2.7 we see the data for the experiments shown in Fig. 2.6. The QCM works by monitoring the frequency of the crystal, and assuming any changes in frequency are due to added mass. However, the frequency is also affected by temperature, and it is radiative heating from the cathode which causes the oscillations seen in the data. The actual amount of cesium deposition is the underlying slope in the graphs.
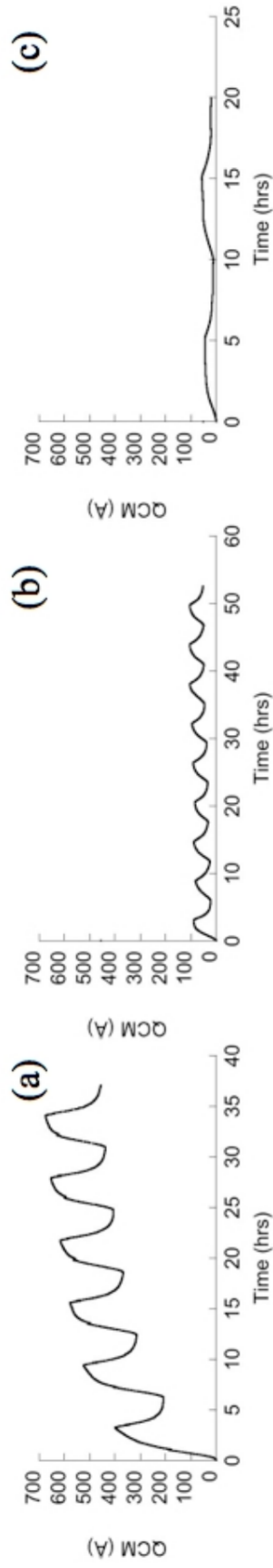
Figure 2.7: Cathode-facing quartz crystal microbalance (QCM) data at (a) 325°C, (b) 150°C, and (c) 125°. Plots (b) and (c) are for the thermal cycling experiments in Fig. 2.6. The periodic oscillations are due to radiative heating of the QCM. The underlying slope is the cesium deposition on the QCM [23].

To determine the total amount of cesium leaving the cathode surface (not just that hitting the QCM), a cosine-squared dependence on the angle from normal to the cathode surface is assumed. With the total cesium mass flow rate, we can estimate the lifetime of the cathode, as seen in Table 2.2. For the equilibrium temperature of $125°C$, the estimated lifetime is 31,000 hours [23].

2.3.3 Contamination Testing

To test the robustness of the cathode, we ion cleaned the cathode surface for 10 minutes, delivering 100 μA of Ar ions at 5 keV. We then gently heated the cathode, and QE peaked at 0.08% at 375 nm. The heater was turned off, and the final QE at room temperature was about 0.06%.

This is the state the cathode is in at the beginning of the graph in Fig. 2.8. A sapphire leak valve was opened to admit 10^{-6} Torr of atmosphere into the vacuum chamber. The total of 110 Langmuirs introduced to the system was composed of 78% N_2, 14% O_2, 3.4% H_2O, 2.6% Ar, 0.9% H_2, and 0.1% CO_2 as measured by a residual gas analyzer. QE dropped to 15% of its initial value in 10 minutes.

	325°C	150°C	125°C
Measured Cs Flow Rate [μg/cm^2/hr]	6.4	0.82	0.023
Cs Monolayer Flow Rate [ML/hr]	95	12	0.34
Est. Reservoir Lifetime [hr]	110	870	31,000

Table 2.2: Measured cesium flow rates and estimated reservoir lifetimes [23].
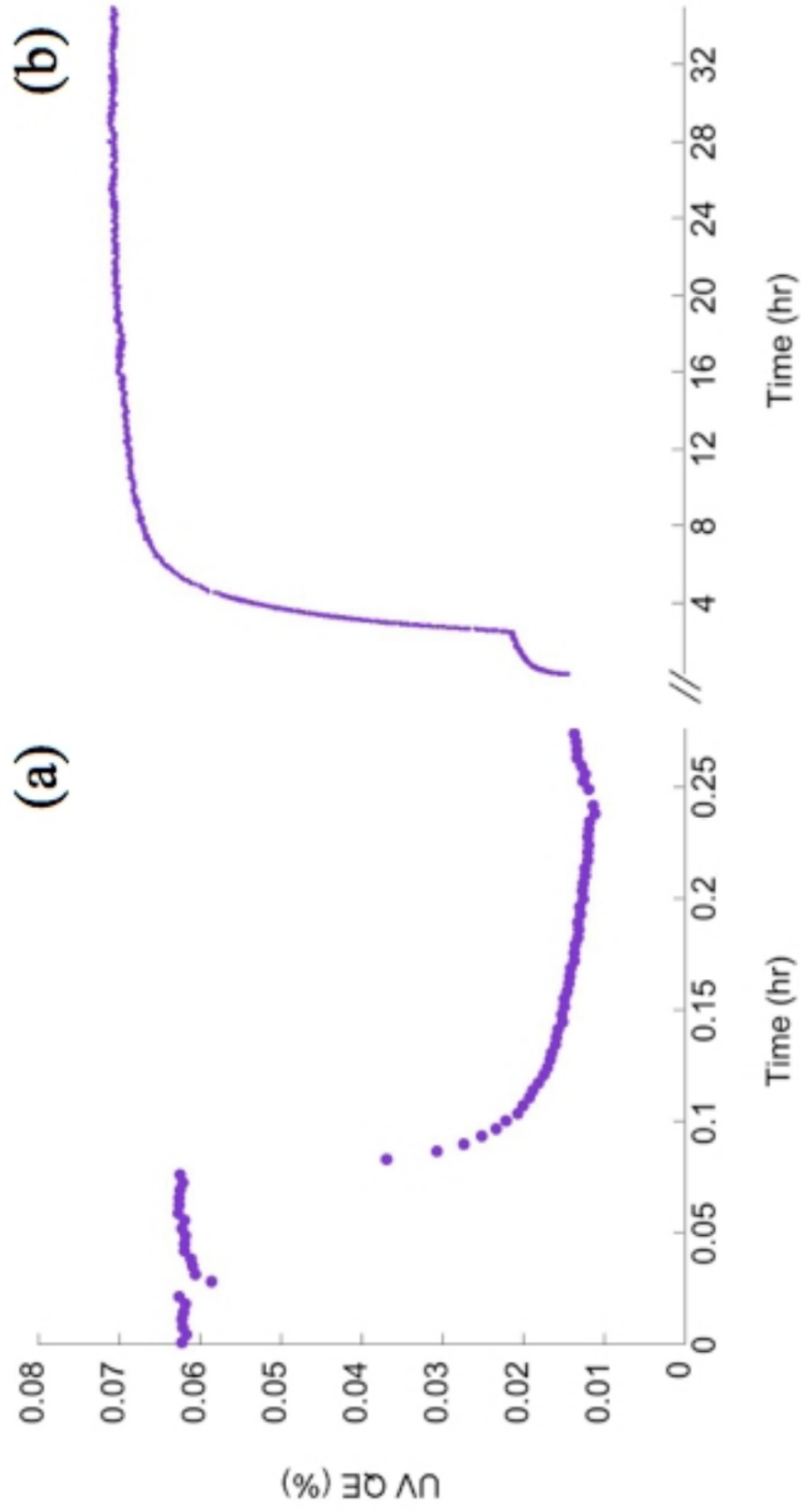
Figure 2.8: In (a), the already cesiated cathode is exposed to air by opening a leak valve, dramatically decreasing QE. In (b), the QE recovers after using the cesium reservoir to replenish the cathode surface [23].

The inflection near 0.25 hr is where the leak valve was closed. An ion pump had remained running during the exposure, so pressure dropped to the nTorr level in a minute. Over the next 3 hours, there was a slight rise in QE. This is due to the rearrangement of the cesium atoms remaining on the surface to a more favorable coverage.

The cathode was then heated to 90°C. Adsorbed contaminants evaporated, cesium diffused to the surface, and QE immediately began to recover. Over the course of several hours, the QE rose to about 0.07%. This improvement over the QE at the beginning of the graph, which was at room temperature, is due to the difference in temperature.

After cooling to room temperature, the QE returned to 95% of its initial, pre-poisoning value. This process of contamination and recovery was repeated multiple times with the same result [23].

Following these experiments, we removed the cathode, and worked on the test stand. When we were finished 9 hours later, we re-installed the cathode and followed our usual bakeout procedure. We heated the cathode to over 500°C for two days, then let it cool to room temperature. As it cooled, we saw photoemission again. At room temperature the QE was 0.03% at 375 nm. When we heated the cathode to 150°C, the QE peaked at 0.06%[*].

_____

[*]Section 2.3 is based on work done by the author. This work is also described in the co-authored paper [23].

2.4 Conclusion

The hybrid-diffuser, controlled porosity dispenser photocathode has done remarkably well in initial tests. The cathode can recover after extreme contamination events. The rate of cesium diffusion to the cathode surface matches the cesium evaporation rate at 125°C. At this temperature, the flow rate of cesium is only a third of a monolayer per hour, and we predict the cesium reservoir to last for 30,000 hours.

The work function-lowering property of cesium also applies to RF cavity walls, so there is an increased risk of arcing if there is too much cesium contamination. We now have data on the cesium evaporation rates from this cathode, which we can use when approaching groups to use the cathode in a photoinjector.

An advantage of the sintered tungsten wire cathode is that several cathodes can be made in one batch of sintering [15], so we are free to try depositing different materials to increase QE. We are particularly interested in multi-alkali and antimony-based cathodes and want to see if they will work with our hybrid dispenser design. An osmium-ruthenium coating, such as used in thermionic cathodes, may increase QE. Gold should also be compatible, since cesium readily diffuses through it, as discussed in Chapter 4. The emission uniformity of the cathode will be discussed in the next chapter. This prototype has shown great promise, and there are many exciting avenues of research to explore.

Chapter 3: Quantum Efficiency Mapping with a Digital Micromirror Device

3.1 Introduction

An electron beam's quality is fundamentally limited by its attributes at the cathode. The emission from photocathodes can be bright, but not necessarily uniform. Quantum efficiency (QE) maps generated by selectively illuminating the cathode surface reveal this non-uniformity. In this chapter a proof-of-principle experiment is described in which a high-resolution map of the QE is generated using a digital micromirror device (DMD). We show a substantial improvement over the best results reported for laser raster scanning.

Photocathodes are promising electron sources for high performance free electron lasers and future accelerator-based light sources [24]. However, no single cathode can simultaneously meet all demands on quantum efficiency (QE), lifetime, emittance, brightness, and response time. Alkali-based cathodes achieve good QE and brightness, whereas metals are superior in long life and fast response time [25]. The emittance of the electron beam generated from a cathode only worsens during transport due to nonlinear forces, so advances in electron beam quality can only be

driven by trade-offs such as emittance exchange, or by better understanding desired electron emission properties such as intrinsic emittance and uniform current density.

The initial transverse current density profile is driven in part by the variation in photoemission (variation in QE) at the cathode surface. Local variation in surface structure, adsorbed contaminants, or stoichiometry can drastically affect local photoemission. In practice, measured QE is a weighted average over the illuminated area, with the weighting determined by the transverse laser intensity profile. QE can be mapped by using a laser spot size smaller than the diameter of the drive laser used for electron beam generation. If two different cathodes have the same average QE over the typical drive laser spot size, a QE map generated with a smaller laser spot size can determine which is more uniform. If the drive laser spot is smaller than the cathode and there is freedom in choosing the photoemission site, a QE map of the full cathode can reveal favorable positions for illumination.

QE maps with very small distances (10 nm) between adjacent points can be measured using photoemission electron microscopy (PEEM) [26,27], but this method requires either the cathode to be moved to a separate apparatus, or PEEM built into the system. The latter is not feasible for accelerators. Alternatively, raster scanning a focused laser spot across the cathode surface can be performed *in situ*. QE maps generated in this way are quantified with the laser spot size and the laser step size. The step size is the center-to-center distance between adjacent points on the QE map. Spot sizes of 200 μm to 1 mm full width at half maximum (FWHM) and step sizes of 40 to 500 μm have been reported in the literature [28–32]. More recent work [32] on *in situ* laser raster scanning of photocathodes demonstrates a

71-μm FWHM laser spot and 30-μm step size, but reports a QE map using larger parameters.

Published practice for raster scanning uses a step size equal to or smaller than the spot size [28–32]. A smaller step size results in overlap between neighboring measurement positions, so a QE map generated in this way is smoother than what would be seen if the spot size could be reduced to the step size. Literature for raster scan QE maps often ignores this smoothing and uses the term resolution to refer to either step size or spot size. We will avoid confusion in this paper by referring individually to step size and spot size rather than resolution.

We report a new method of generating QE maps which uses a Texas Instruments digital micromirror device (DMD). We use the DMD to produce pixel level maps with a 47-μm FWHM spot size and a 16-μm step size, the smallest of any QE mapping method yet reported in the literature suitable for *in situ* measurements in photoinjectors[*]. Other advantages of using a DMD for mapping QE are simplicity and speed. Our DMD array can be refreshed at rates up to 9.8 kHz.

3.2   Experimental Setup

The measurements reported here use a Texas Instruments DMD "Discovery 1100," a 1024 x 768 array of micromirrors physically integrated with a control board. The total size of the array is 14.0 by 10.5 mm. The DMD is controlled by a Universal

---

[*]The idea to use a DMD to map the QE of a photocathode was first demonstrated at Brookhaven in 2006 [33], albeit with large spot sizes (where each point in the QE map was illuminated by a block of 64x64 DMD micromirrors instead of the single micromirrors used here), but to the author's knowledge has never been reported in the literature or conference proceedings. We independently conceived the idea to use a DMD for QE mapping.

Serial Bus (USB) connection to a Windows PC. The distance between the centers of neighboring micromirrors (the pitch) is 13.68 μm, which includes a 1-μm gap between mirrors. Each mirror can be individually flipped to one of two stable positions 12 degrees from normal via electrodes under two of each mirror's corners (Fig. 3.1).

The cathode used for proof-of-principle QE maps is cesiated tungsten of the controlled porosity reservoir design being investigated at the University of Maryland [15]. The goal of this design is to increase both electron emission uniformity and cathode lifetime. The cathode was intentionally contaminated prior to mapping to partially deplete QE and increase local variation in emission. The chamber pressure while mapping is 3×10^{-10} Torr. The spatially averaged QE is about half that corresponding to the ideal cesium sub-monolayer work function minimum [23].

The optical arrangement is similar to that previously reported for beam halo imaging [35]. A simplified experimental schematic is shown in Fig. 3.2. A 405 nm CW laser (CrystaLaser BCL-100-405) illuminates the DMD, which is 62 cm away. The laser has variable output from 3 to 100 mW. The reflected laser light from the DMD has a 2D diffraction pattern. An aperture blocks all but the central order spot since the higher order spots diverge enough to be clipped by the 1 inch diameter optics before reaching the cathode. The central order spot has 16% of the power incident on the DMD. The transmittance/reflectance of the optical elements are shown in Table 3.1. The light from the DMD is simultaneously imaged onto the photocathode and onto a frame-transfer CCD camera. The SBIG ST-402ME model camera is fan-cooled and has a 765 by 510 array of 9-μm pixels.
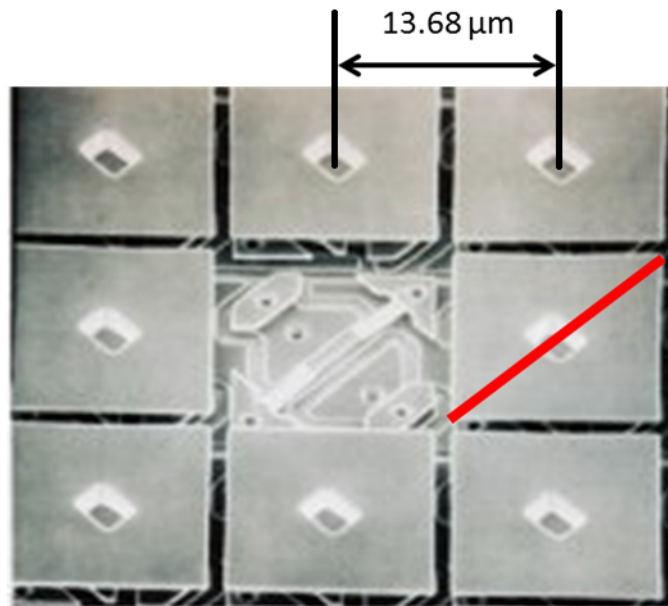
Figure 3.1: Image adapted from Texas Instruments. Magnified view of a DMD. In the center, a mirror has been removed, revealing the underlying CMOS architecture. Each mirror can be rotated about the diagonal axis indicated in the image. The DMD used in the experiment consists of a 1024x768 array of mirrors. To make the two stable mirror positions correspond to reflecting incident light horizontally, the DMD is rotated so that the mirror diagonal is perpendicular to the benchtop [34].
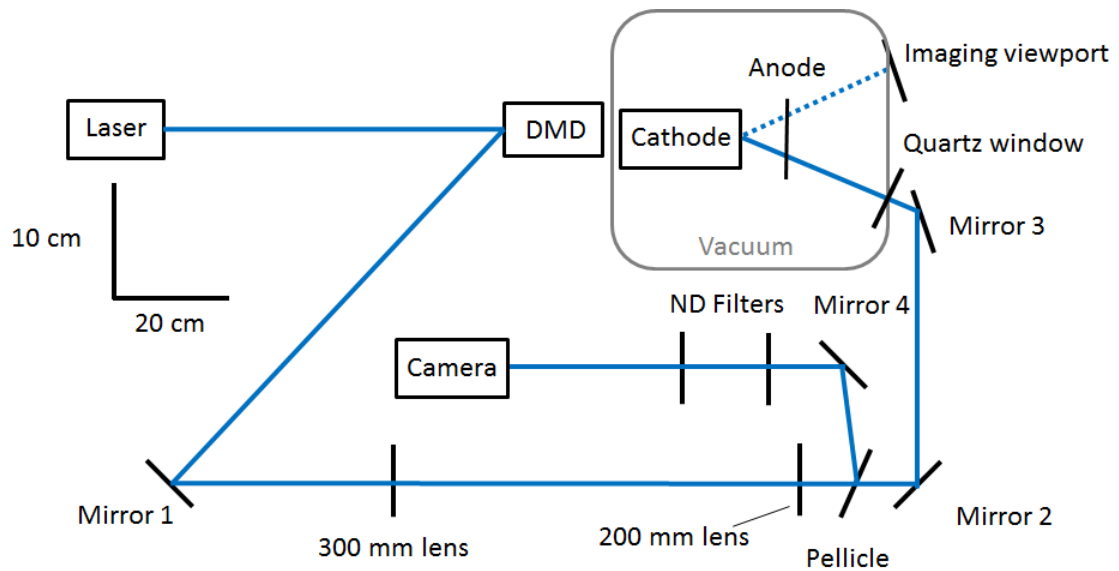
Figure 3.2: A schematic of the experimental setup. The DMD selectively reflects a small cross-section of the incident laser beam through the rest of the optical components to the cathode. The camera and cathode are the same distance from the pellicle, which allows us to deliver 96% of the laser beam's power to the cathode and image 4% with the camera. The scale is for the placement, not the size, of optical elements.

Table 3.1: Transmittance and Reflectance [34].

Optical Element	Transmit./Reflect. (%)
DMD (central order reflection)	16
Mirror 1	89
Lenses 1 and 2 (per lens)	96
Beam Splitter (to cathode)	96
Mirrors 2 and 3 (per mirror)	83
Quartz window	93
TOTAL	8.1

A two lens relay system focuses light on the cathode. Lens 1 (200 mm focal length) is located 107 cm from the DMD. Lens 2 (300 mm focal length) is located 65 cm away from Lens 1. Both the cathode and the CCD camera are 84 cm away from Lens 2. The Melles Griot biconvex UV fused silica lenses have an anti-reflective coating for 355-532 nm light. An individual micromirror or a micromirror group can be selected to reflect a portion of the laser beam through the remaining optics. During alignment, the DMD is set to reflect a checkerboard pattern. Lens 1 is adjusted until the pattern on the cathode is in focus when seen through the imaging viewport. A pellicle beam splitter reflects 4% of the beam power to the CCD. With the CCD and cathode equidistant from the beam splitter, the CCD position is adjusted to find the sharpest focus. Neutral density filters (total of optical density 3) are used to avoid saturating the camera.

The incident optical power is determined for each QE measurement. The reflection from a single illuminated DMD pixel is detectable with the CCD camera but falls below the threshold of our thermopile (0.1 mW). Thus, it is necessary to use the CCD to measure lower power levels; this additionally allows higher-speed laser power profiling. The CCD has a pixel response variation of less than 0.3%. The integrated CCD count is correlated with laser power by capturing the entire laser spot with the CCD while varying the laser power. Performing a linear fit calibrates the CCD single-pixel response so that integration of acquired images reveals the optical power incident on the cathode.

The photocurrent is observed to vary linearly with laser power. This means that our measurements are not space charge-limited. Since QE is proportional to

current divided by power, variations in power from different DMD pixels have no effect on QE. Photocurrent is measured using a Keithley Model 486 picoammeter in series with the 6 mm diameter cathode and an anode 1.6 mm away from the cathode. A bias of 160 V is applied between cathode and anode using a simple series of (nominally) 9V batteries. This isolated voltage supply, as well as triaxial cable, minimizes noise. The low noise is necessary to permit measurement of the average 80 pA photocurrents generated when using single DMD pixels.

3.3   Results

QE maps are made with different step sizes by programming groups of DMD pixels to switch together. Maps using DMD pixel groups of 9x9, 3x3, and 1x1 correspond to step sizes of 148, 49, and 16 μm, respectively. The 16-μm step size map covers only a subset of the larger step size maps for faster acquisition time. As shown in Fig. 3.3, the 16 and 49-μm step size maps are sub-averaged to allow direct comparison to the 49 and 148-μm maps, respectively. The average QE, as measured using a single 27x27 group of DMD pixels, is comparable: $(0.052 \pm 0.001)\%$ for the 148 and 49-μm step size maps. The average QEs of the 16-μm step size map agree with the corresponding QEs on the 49-μm step size map to within 0.002% QE. These spatial fluctuations are attributed to the polycrystalline porous tungsten surface of the cesium dispenser cathode under test.

The point spread function of the optical relay system is obtained by imaging a single micromirror with the laser. The horizontal and vertical profiles are fit to
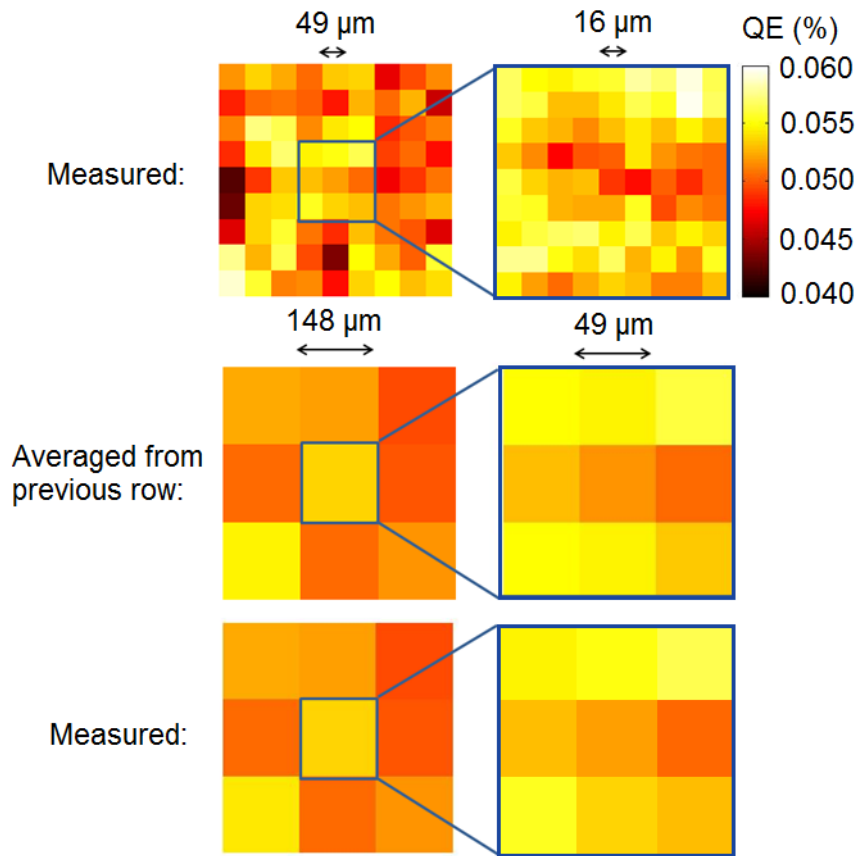
Figure 3.3: Quantum efficiency (QE) maps. Maps in the right column are magnified by 3:1 compared to their corresponding areas in the left column. The second row shows average maps of the first row, which can be compared to the measured maps of the third row. The first row uses 49-μm step sizes on the left and 16-μm step sizes on the right. The second and third rows use 148-μm step sizes on the left and 49-μm step sizes on the right [34].

Gaussians, each with a 47-μm FWHM. We measure a step size of 16 μm by individually imaging neighboring DMD mirrors (Fig. 3.4). This step size is consistent with the pitch of the DMD mirrors, and the 1.2 magnification from the DMD to the cathode.

3.4   Conclusion

QE maps are characterized by step size, spot size, and ease of generation. PEEM offers the smallest distance between adjacent points on a QE map, but requires the cathode to be removed from a photoinjector. Laser raster scanning can be done in place, but only permits measurements with a single laser spot size barring significant optical realignment. We have demonstrated that a DMD can be used for variable step size QE mapping, which allows for a quick large step size (150 μm) map of the entire photocathode surface followed by a small step size (16 μm) map of the smaller region to be illuminated for photoinjection.

A larger field of view is possible if sufficient power is transmitted to the cathode when the laser beam is expanded to fill the DMD. Power to the cathode could be increased by redesigning the system so as to accept higher-order diffraction spots reflected from the DMD. A chopper and lock-in amplifier were tested, and could be used to detect smaller photocurrents, but were not needed for the results presented here. Power measurements are currently not a concern, since the CCD can easily detect per-pixel laser power three orders of magnitude less than reported here. DMD mirror switching, laser power and photocurrent measurements have been automated
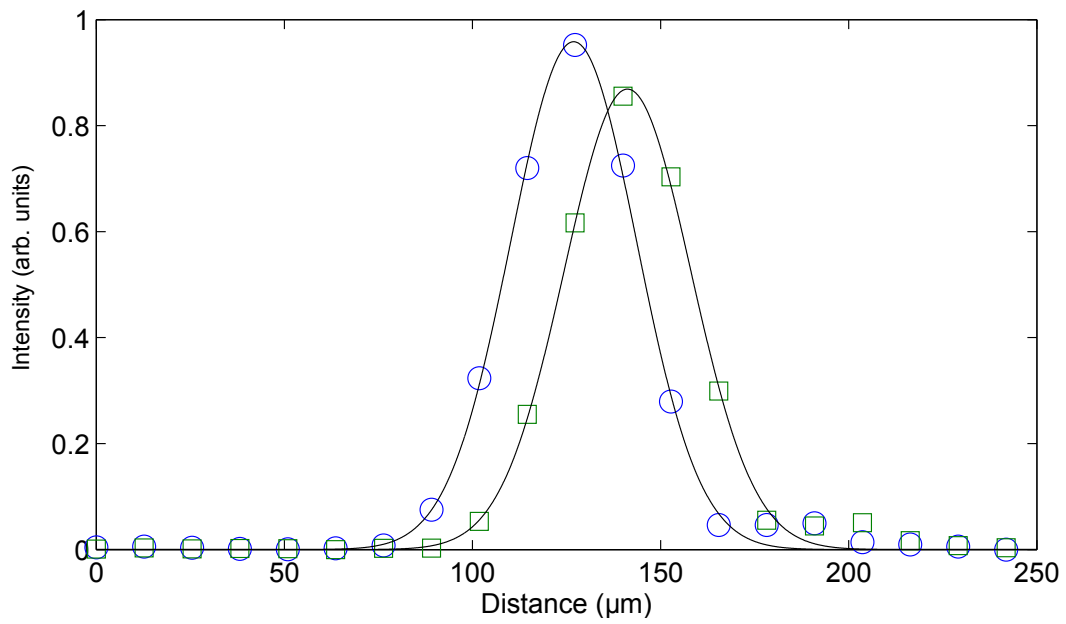
Figure 3.4: The peaks from two neighboring DMD mirrors are 16 μm apart. Since the measurements are not space charge limited, the difference in power from the two mirrors has no effect on measured QE [34].

to accommodate the increased number of data points for small step size, large field of view maps. A screenshot of this program is shown in Figure 3.5.

Commercially available DMDs are at present not optimized for sub-320 nm use. However, with the advent of new advances in DMD fabrication and/or the use of windows which are transmissive down to 266 nm, DMDs may soon be available for measuring QE in the deep UV with small step size [36]. Such a capability would allow a direct application of the technique presented here to cathode materials such as copper.

The DMD permits the generation of a QE map with a step size of 16 μm and a spot size of 47 μm, which betters the lowest reported by laser rastering. The DMD allows rapid *in situ* QE mapping without the need to move the drive laser or any other optical components. QE map step size and laser spot size can be easily adjusted. This is a promising method for probing the spatial electron emission characteristics of photocathodes[*].

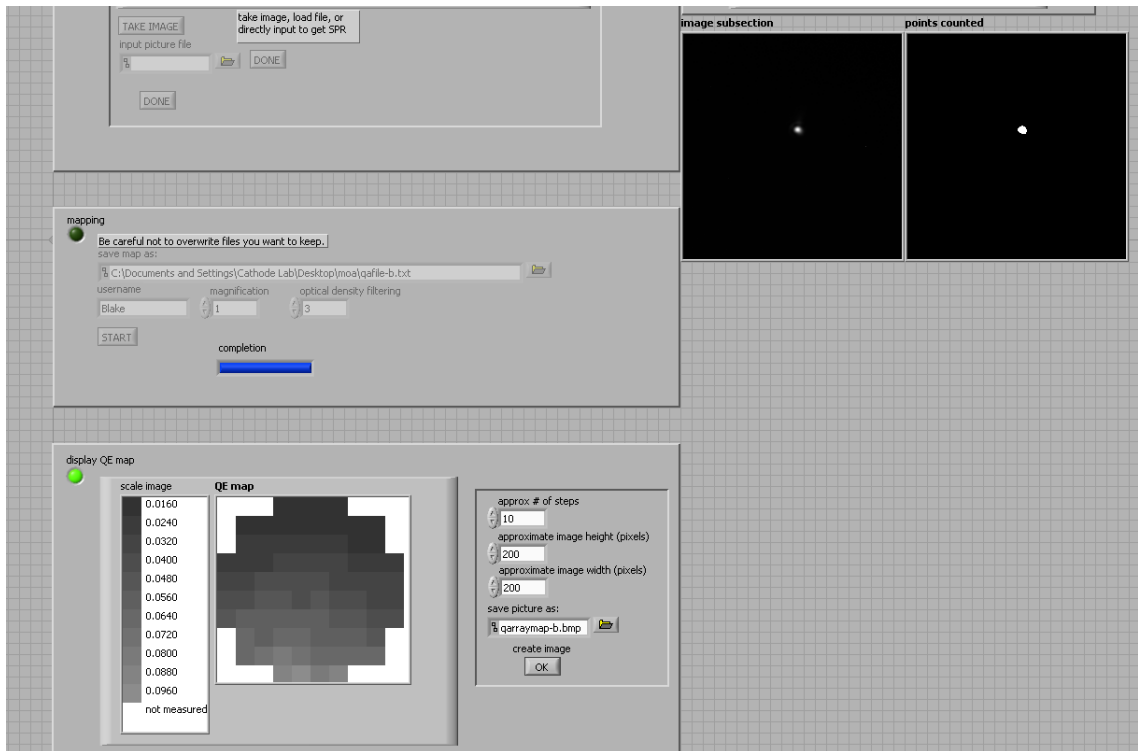Figure 3.5: Automated QE mapping program. Simulated photocurrents are used for low drive laser power testing, but the powers are measured. For the two images in the upper right corner, the left image is that recorded by the camera. The right image shows what region the software is including in its integration to calculate total power. The QE map on the lower left is generated using the simulated currents and measured powers.

Chapter 4: Cesium Auride

4.1 Introduction

We have so far extended the lifetime of a cesiated tungsten cathode, and developed a technique for measuring the uniformity of quantum efficiency. In this chapter, we address the most fundamental aspect of photocathode research – testing new cathode materials. We focus on cesium auride, which we have shown to have a quantum efficiency of 0.7% at 532 nm, and which we believe will be compatible with our hybrid cesium diffuser design discussed in Chapter 2. This QE is more than an order of magnitude greater than that found in previous experiments.

These results are promising for use in a megawatt-class free electron laser, which calls for a cathode capable of delivering 2% QE for a green drive laser [24]. The current state of the art in FEL output power is 14 kW at Jefferson Lab. The photocathode is one of the limiting factors for increasing output power, so being able to provide a long-lasting cathode with good green QE would be a major advancement.

Gold is well suited for use with our hybrid dispenser because of cesium's unusual interaction with gold. For most bulk metals, cesium will remain on the cathode surface. Typically 50 to 60 percent of a monolayer coverage leads to the dramatic

increases in QE due the dipoles formed. With gold, however, cesium forms an intermetallic alloy and develops semiconductor properties [37]. So cesium affects not only the surface of gold, lowering the effective work function, it also improves the likelihood of a photo-excited electron reaching the cathode surface, as discussed in Chapter 1.

4.2   Experimental Setup

To perform our experiments with cesium auride, we constructed the gold evaporation system seen in Figure 4.1. An electric current of 84 A was run through a molybdenum (Mo) boat holding gold pellets. (We first used a boat made of tantalum, but at high temperature a hole formed in the boat, and we did not evaporate gold.) The gold evaporated onto a tungsten cathode which was held in place with a steel ring inside the vacuum chamber and a magnet outside. The cathode was on a viewport which allowed us to see the boat and let us know when gold started to evaporate.

20 minutes after the gold started to evaporate, the viewport was opaque. After a total of 44 minutes of evaporation, we stopped running current through the boat. At this point, pressure in the turbo-pumped system was 10^{-4} Torr.

We removed the cathode and used profilometry to scan the boundary between gold-coated and uncoated regions at several points. The gold layer was 500 ± 50 nm, and covered all of the cathode except for the outer edge which was shielded by the steel ring.
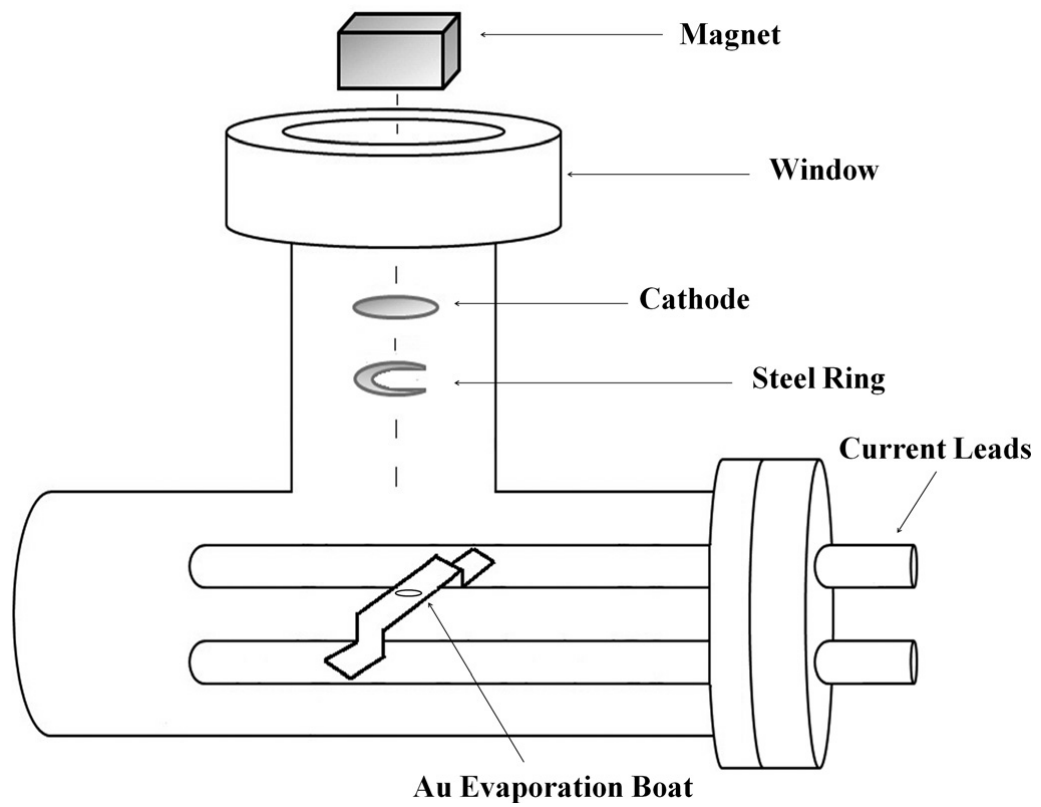
Figure 4.1: Gold evaporation system [38].

The cathode was placed in our QE test stand, and we followed our usual bakeout procedure. The cathode was heated to 700°C. After letting the cathode cool, the ion-pumped chamber pressure dropped to 2 nTorr.

When heated, a cesium bismuth source pointed at the cathode releases elemental cesium. A quartz crystal microbalance near the cathode and facing the source allows us to measure the amount of cesium deposited on the cathode surface.

Five small CW lasers on a computer-controlled single-axis robotic stage illuminate the cathode in turn, allowing the measurement of QE from the near-IR to the near-UV. The lasers have powers on the order of 10 mW, and their wavelengths are 808, 655, 532, 405, and 375 nm.

4.3   Results

We deposited 330 nm of cesium on the cathode, causing an increase in QE which eventually peaked and decreased again, as seen in Figure 4.2. This behavior of the QE is similar to what is observed in metals like tungsten, but requires far more cesium. For tungsten, we see a similar curve using only 1 nm of cesium.

More cesium is needed because it is diffusing through the gold. As the cesium moves farther into the gold, it is forming the intermetallic alloy with semiconductor-like properties. As discussed in Chapter 1, this means there is less electron-electron scattering, so a photo-excited electron has a better chance of reaching the cathode surface. Since the longer wavelength photons penetrate deeper into the cathode as seen in Figure 4.3, it takes more cesium to form the intermetallic alloy to this depth
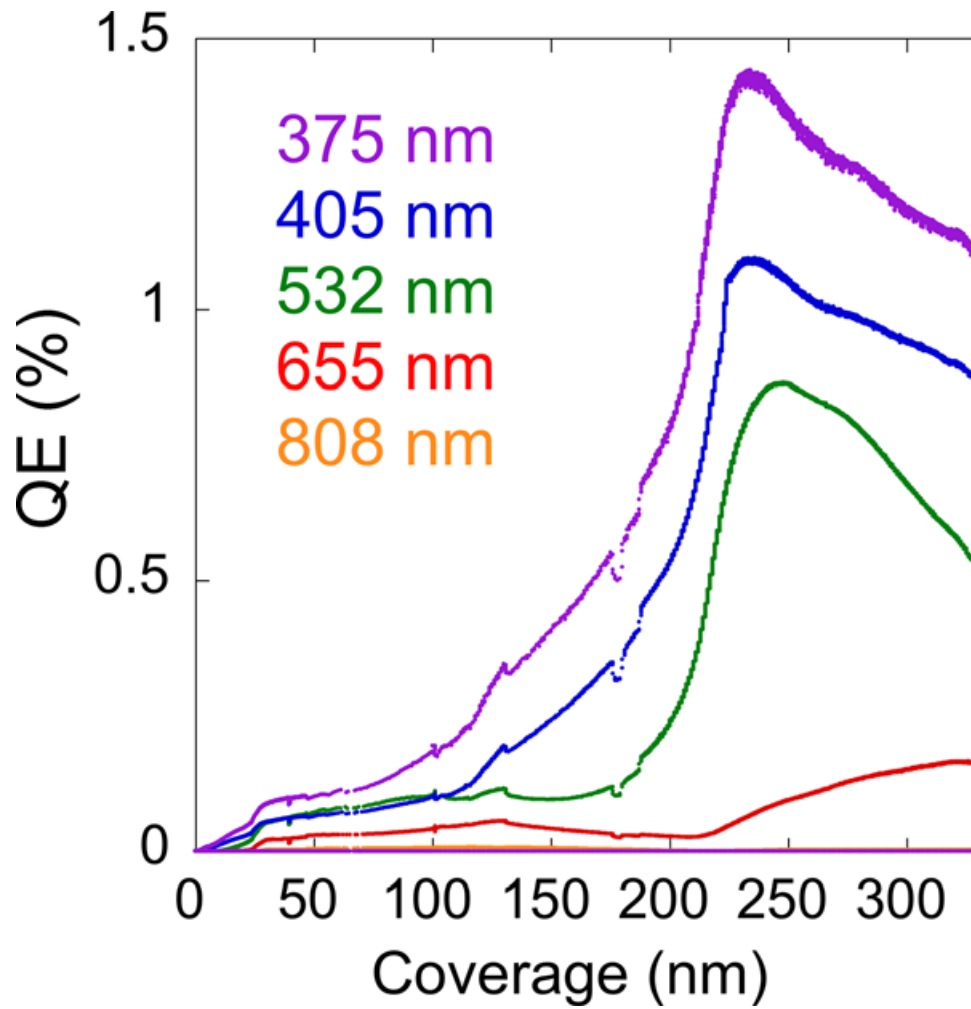
Figure 4.2: Quantum efficiency goes through peaks as more cesium is deposited. Data was taken for the five wavelengths indicated. There was some photoemission at 808 nm but the QE peaked at 0.0001%. The QE is highest for the highest photon energy 375 nm light, and is successively lower for the longer wavelength lights [38].

from the cathode surface. Evidence of this effect can be seen in Fgure 4.2, where the UV (375 nm) QE peaks first, since the light has the shortest penetration depth. The other QE peaks are in increasing penetration depth order, seen most dramatically for red light (655 nm).

By watching when photoemission began for each wavelength of light, we could tell what the work function of the cathode was at those points, as seen in Figure 4.4. The work function of the cathode was less than 1.53 eV, which is the energy corresponding to 808 nm light.

Cesium auride was previously studied by Spicer in the 1960s [40], but no further study was conducted due to the low QE as seen in Figure 4.5. We attribute the discrepancy in QE to the differnce in preparation method. Spicer was attempting to grow cesium auride with a 1:1 stoichiometry. We do not know what are stoichiometry was, but our results indicate it is much more favorable for photoemission.

4.4   Conclusion

Our results with cesium auride so far encourage further testing. A future series of tests will try testing cathodes with different thicknesses of gold, with the goal of maximizing quantum efficiency. To this end, we designed and machined the multi-cathode holder shown in Figure 4.6, which allows us to reduce the number of vacuum breaks needed. Furthermore, our robotic stage allows us to measure QE of either set of three cathodes in a line just by inserting the corresponding stage coordinates into the LabVIEW program. (The lasers would have to be re-aligned
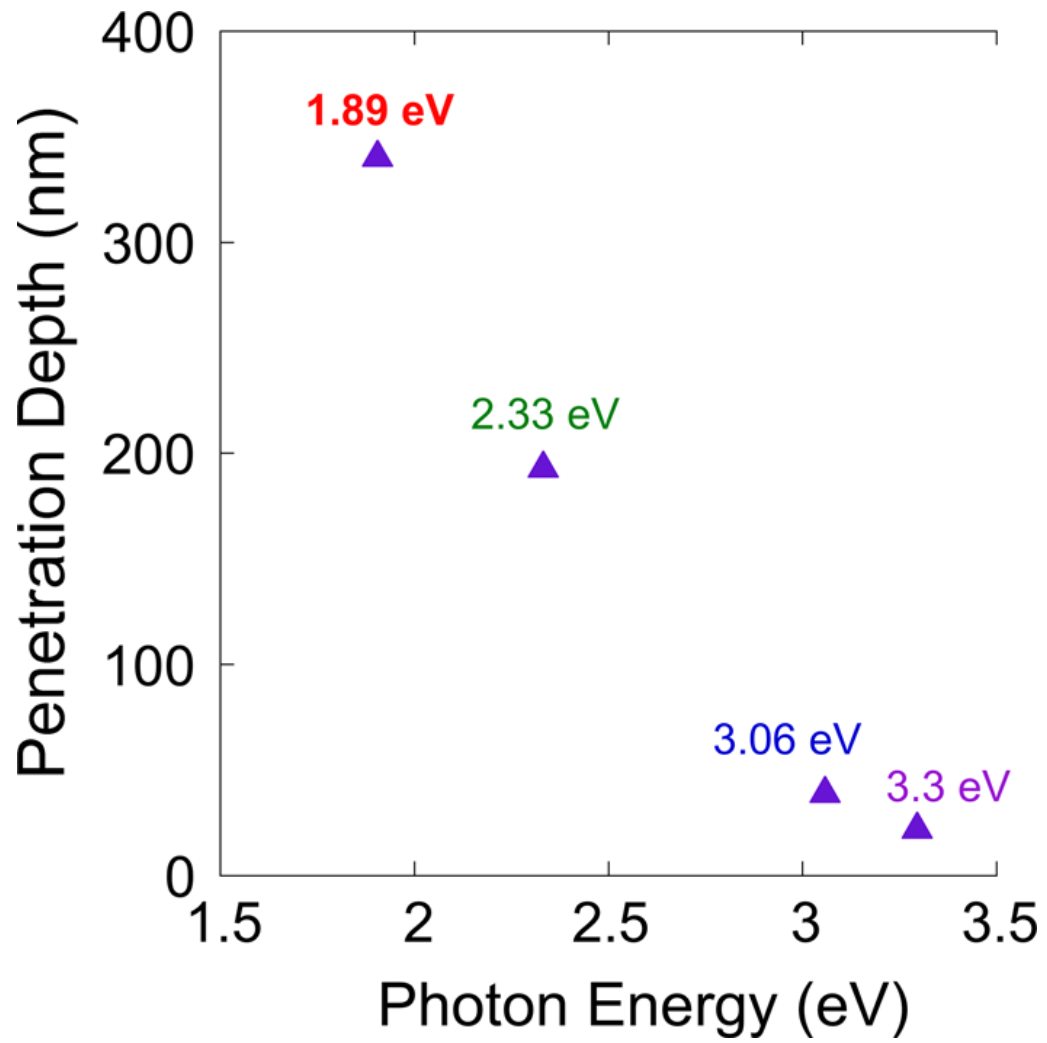
Figure 4.3: Penetration depth data from [39] for different photon energies [38].
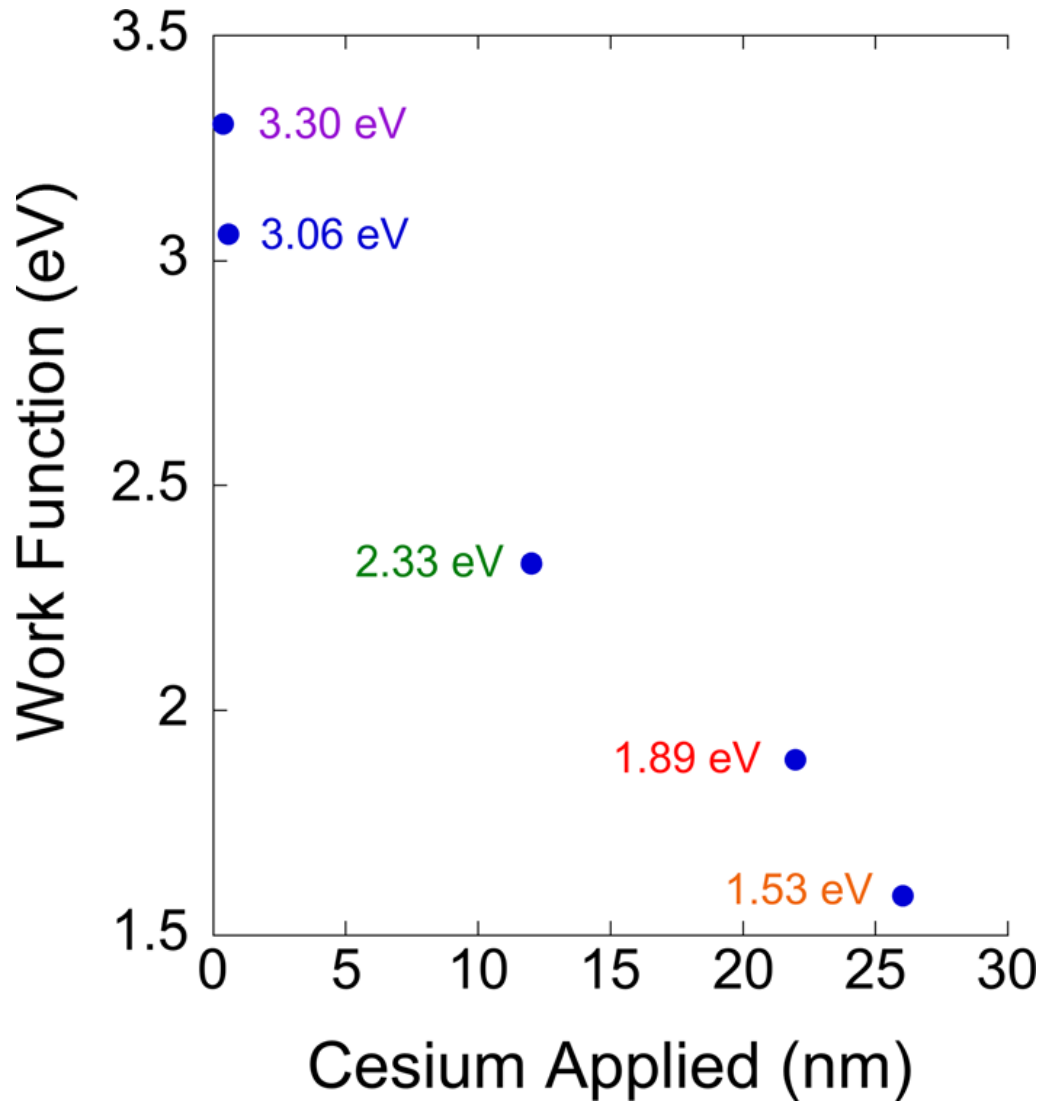
Figure 4.4: Photoemission thresholds indicating the cathode work function at those points. From this we know the final work function of the cesium auride cathode was less than 1.53 eV [38].
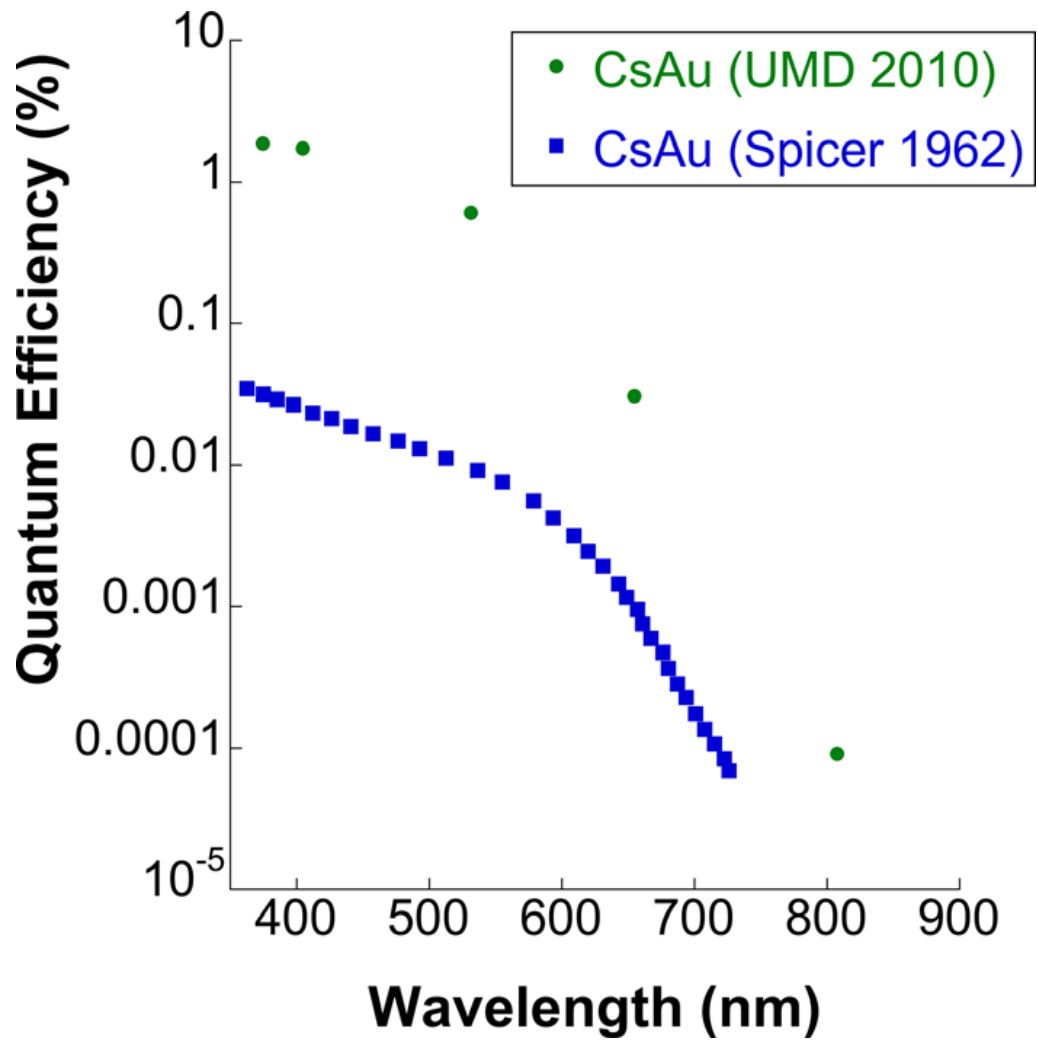
Figure 4.5: Quantum efficiency of cesium auride from Spicer [40] and UMD [38].

to hit the second row of cathodes.) We can use this cathode holder to test different fabrication recipes on relatively inexpensive tungsten cathodes. Once the ideal gold thickness if found, we can then test cesium auride with the hybrid diffuser cesium reservoir discussed in Chapter 2.

The ready diffusion of cesium through gold indicates that a cesium auride cathode should be compatible with a cesium reservoir. We have already shown a QE of 0.7% for green light, and we could potentially increase this number through optimizing the thickness of gold. Cesium auride is a promising candidate for a high-QE, long-lifetime photocathode*.

---

*This chapter is based on work done by the author. This work is also described in the co-authored paper [38].

Figure 4.6: Custom-designed and machined multi-cathode holder allows 6 cathodes to be tested with only one vacuum break. The cathodes are held in place with set screws.

Chapter 5: Conclusion

Through the work described in this dissertation, we have advanced the study of photocathodes. Our hybrid diffuser cesium reservoir photocathode has shown great robustness and long lifetime. Scanning quantum efficiency across a cathode's surface with a DMD is permits high resolution, *in situ* maps to be made. Our rediscovery of cesium auride and its compatibility with our cesium reservoir indicates that it is a strong candidate for a high QE, long-lifetime photocathode.

5.1   Summary of Results

5.1.1   Hybrid Diffuser Cesium Reservoir Photocathode

We have advanced the pioneering work on cesium reservoirs already performed at UMD [10]. We already knew that a cesium reservoir could be used to restore the sub-monolayer coating of cesium to the surface of a sintered tungsten powder cathode, thus allowing QE to remain high. By adding a second layer composed of sintered tungsten wires, the gaps between which are uniformly distributed pores, we are able to more evenly distribute cesium on the cathode surface. The sintered tungsten powder layer acts to limit the diffusion rate of cesium, which our modeling

showed would be too high if only the sintered wires were used.

We were able to rejuvenate our hybrid dispenser cathode many times. Even after allowing the already activated cathode to sit in air for several hours, we were still able to return the cathode to UHV and replenish the surface, returning elevated QE. At the optimum operating temperature 125°C, our measurements indicate a predicted lifetime of 30,000 hours. The cesium flow rate when hot is a third of a monolayer per hour. For our QE test stand, we do not need to worry about this rate. However in a photoinjector, where the electrons would be accelerated to high energies, cesium can lower the work function of cavity walls, thus increasing the risk of electric breakdown (arcing).

5.1.2   QE Mapping with a Digital Micromirror Device

Mapping the quantum efficiency of a photocathode, as well as knowing the profile of the drive laser, allows one to determine what the initial transverse distribution of electrons will be. QE maps are usually made via *in situ* laser raster scanning, or by PEEM in a separate apparatus.

Our DMD-generated QE maps are made with a step size of 16 μm and 47 μm FWHM spot size, which is an improvement over conventional maps made with laser raster scanning (step size 40 μm, spot size 200 μm). Another benefit of using a DMD is that scanning resolution can be easily changed without needing to adjust optics by using groups of DMD mirrors instead of single mirrors for each point in the QE scan.

5.1.3 Cesium Auride

While cesiated tungsten has much higher QE than bare tungsten, its peak QE is only 0.03% for green light. Cesium diffuses through gold, instead of remaining on the surface as with most other metals.

In our initial tests, the intermetallic alloy of cesium auride has a peak QE of 0.7% for green light. Furthermore, cesium auride should be fully compatible with our cesium reservoirs, thus allowing for a long lifetime.

5.2 Future Work

There is still more work to be done to follow up on the results presented here. An osmium-ruthenium coating has long been used in the thermionic cathode community to increase the electron yield, so we would like to test this coating with our hybrid diffuser desgin. Alkali antimonide cathodes like Na_3Sb also have high QE, and should be tested for compatibility with our cesium reservoir.

While our QE maps made with a DMD offer good resolution, advances need to be made before larger field of view maps can be generated. Our drive laser currently only covers a small area of the DMD surface. If we expanded the beam to cover the whole surface, with our setup we would not be able to measure the smaller photocurrents when using single DMD mirrors. To deliver more power to the cathode, we could use a higher-power laser. We could also redesign the optics to capture higher-order diffraction spots from the DMD (we currently only capture the central, brightest spot). In our measurements, we had to use an OD 3 neutral

density filter to avoid saturating the camera used to monitor the laser power and position, so we should be easily able to measure optical powers three orders of magnitude smaller.

Our initial tests with cesium auride are very promising, but there is room for improvement. We arbitrarily chose a thickness of gold much larger than the optical penetration depth of cesium. We should be able to repeat the results using less gold, and we should investigate thicknesses at or less than the penetration depths for higher QE.

5.3 Final Thoughts

Photocathodes offer several stengths as electron sources, such as high brightness and the ability to turn emission on and off with the drive laser, which is useful for RF accelerators. When choosing a photocathode, we usually have to decide between long lifetime and high quantum efficiency. Our cesium reservoir cathode design offers the potential to have both.

Appendix A: Emittance

There are several definitions of emittance. We will talk of three definitions of transverse emittance here, but other works may use the same words to refer to different definitions. The three definitions of transverse emittance here are all related to the area occupied by the electrons in trace space. Total x-emittance is

$$\epsilon_{t,x} = \frac{1}{\pi} \iint f(x, x') \, dx \, dx' \tag{A.1}$$

with $f(x, x')$ being the distribution of electrons.

An issue with total emittance is that it is conserved under both linear and nonlinear forces. In Fig. A.1, the total area of occupied phase space is constant, yet the beam at the last time step occupies a greater *effective* area. So we define effective x-emittance to be

$$\epsilon_x = 4\sqrt{\langle x^2 \rangle \langle x'^2 \rangle - \langle xx' \rangle^2} \tag{A.2}$$

with units of mm-mradians. The factor of 4 is so that effective and total emittance are the same for an ideal ellipse. RMS emittance is the same expression without the factor of 4. Effective emittance does increase when the electron beam is subject to nonlinear forces, so it is a better indicator of beam quality. The emittances are summarized in Table A.1.
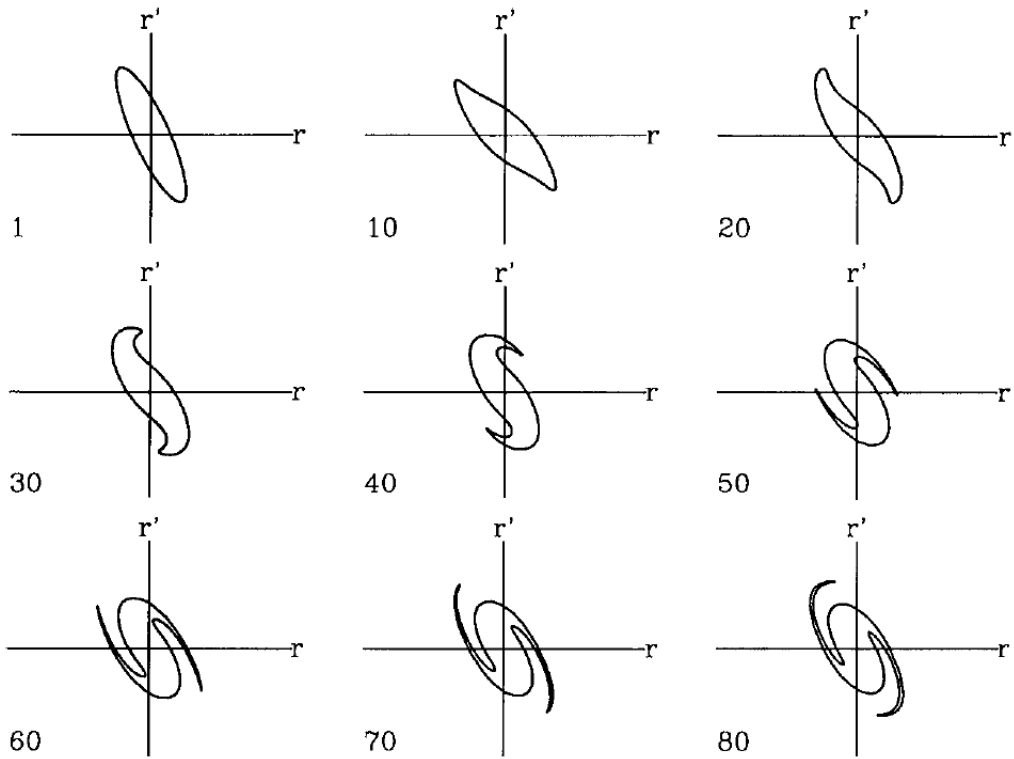
Figure A.1: Progressive distortion of the transverse direction r trace-space ellipse during beam propagation through a periodic channel of thin lenses with spherical aberrations. The numbers associated with each figure indicate the lens periods that have been traversed [12].

Type	Symbol	Conserved under linear forces?	Conserved under non-linear forces?
Total emittance	ϵ_t	Yes	Yes
RMS emittance	$\tilde{\epsilon}$	Yes	No
Effective emittance	$\epsilon = 4 * \tilde{\epsilon}$	Yes	No

Table A.1: Comparison of emittance definitions [41].

Bibliography

[1] A. H. Sommer. The element of luck in research–photocathodes 1930 to 1980. *Journal of Vacuum Science & Technology A*, 1(2):119–124, 1983.

[2] S. Arrhenius. Nobel prize in physics 1921 - presentation speech. `http://nobelprize.org`, 1922. Accessed 18 Jul 2011.

[3] N. Zettili. *Quantum Mechanics: Concepts and Applications*. Wiley, West Sussex, England, 2001.

[4] NIST. Reference on constants, units, and uncertainty. `http://physics.nist.gov/cuu/Constants/`, 2012. Accessed 6 Feb. 2012.

[5] K. L. Jensen. Electron emission physics. In *Advances in Imaging and Electron Physics*, volume 149, pages 147 – 279. Elsevier, 2007.

[6] D.H. Dowell, I. Bazarov, B. Dunham, K. Harkay, C. Hernandez-Garcia, R. Legg, H. Padmore, T. Rao, J. Smedley, and W. Wan. Cathode R&D for future light sources. *Nuclear Instruments and Methods in Physics Research Section A: Accelerators, Spectrometers, Detectors and Associated Equipment*, 622(3):685 – 697, 2010.

[7] W. E. Spicer and A. Herrera-Gómez. Modern theory and application of photocathodes. In *1993 International Symposium on Optics, Imaging and Instrumentation*, 1993.

[8] J. Smedley. Cathode Physics class at the U.S. Particle Accelerator School, 2012.

[9] E.J. Montgomery. *Characterization of Quantum Efficiency and Robustness of Cesium-based Photocathodes*. PhD thesis, University of Maryland, 2010.

[10] N. A. Moody, K. L. Jensen, D. W. Feldman, P. G. O'Shea, and E. J. Montgomery. Prototype dispenser photocathode: Demonstration and comparison to theory. *Applied Physics Letters*, 90(11):114108, 2007.

[11] D. Stratakis. *Tomographic Measurement of the Phase Space Distribution of a Space-Charge-Dominated Beam.* PhD thesis, University of Maryland, 2008.

[12] M. Reiser. *Theory and Design of Charged Particle Beams.* Wiley-VCH, 2008.

[13] K. L. Jensen. Private correspondence, 2012.

[14] E. J. Montgomery, D. W. Feldman, P. G. O'Shea, Z. Pan, N. A. Moody, and K. L. Jensen. Fabrication and measurement of efficient, robust cesiated dispenser photocathodes. In *Proc. PAC 2007*, pages 1206–1208, 2007.

[15] R.L. Ives, L.R. Falce, S. Schwartzkopf, and R. Witherspoon. Controlled porosity cathodes from sintered tungsten wires. *IEEE Transactions on Electron Devices*, 52(12):2800 – 2805, 2005.

[16] R.L. Ives, E. Montgomery, B. Riddick, and L. Falce. Robust, long-life photocathodes for high frequency RF sources. In *Infrared, Millimeter, and Terahertz Waves (IRMMW-THz), 2012 37th International Conference on*, pages 1–2, 2012.

[17] W. Steckelmacher. Knudsen flow 75 years on: the current state of the art for flow of rarefied gases in tubes and systems. *Rep. Prog. Phys.*, 49(10):1083–1107, 1986.

[18] S. Chapman and T. G. Cowling. *The mathematical theory of non-uniform gases: an account of the kinetic theory of viscosity, thermal conduction, and diffusion in gases.* Cambridge University Press, 1991.

[19] K. L. Jensen and Z. Pan. Private correspondence, 2011.

[20] C. B. Alcock, V. P. Itkin, and M. K. Horrigan. Vapour pressure equations for the metallic elements: 298–2500K. *Canadian Metallurgical Quarterly*, 23(3):309–313, 1984.

[21] E. J. Montgomery, D. W. Feldman, P. G. O'Shea, J. C. Jimenez, J. R. Harris, and K. L. Jensen. Cesium emission in dispenser photocathodes. In *32nd International Free Electron Laser Conference*, 2010.

[22] N.A. Moody. *Fabrication and measurement of regenerable low workfunction dispenser photocathodes.* PhD thesis, University of Maryland, 2006.

[23] E.J. Montgomery, Z. Pan, B.C. Riddick, P.G. O'Shea, D.W. Feldman, K.L. Jensen, R.L. Ives, and L.R. Falce. Enhanced lifetime hybrid-diffuser cesium reservoir photocathode. In *AIP Conference Proceedings*, volume 1507, pages 933–938, 2013.

[24] National Research Council Committee on a Scientific Assessment of Free-Electron Laser Technology for Naval Applications. *Scientific Assessment of High-Power Free-Electron Laser Technology.* The National Academies Press, 2009.

[25] K.L. Jensen, J.E. Yater, J.L. Shaw, R.E. Myers, B.B. Pate, J.E. Butler, and T. Feygelson. Bunch characteristics of an electron beam generated by a diamond secondary emitter amplifier. *Journal of Applied Physics*, 108(4):044509, 2010.

[26] A. Scholl. Applications of photoemission electron microscopy (PEEM) in magnetism research. *Current Opinion in Solid State and Materials Science*, 7(1):59 – 66, 2003.

[27] P. U. P. A. Gilbert, A. Young, and S.N. Coppersmith. Measurement of c-axis angular orientation in calcite (CaCO3) nanocrystals using X-ray absorption spectroscopy. *Proceedings of the National Academy of Sciences*, 108(28):11350– 11355, 2011.

[28] J. Gubeli, R. Evans, A. Grippo, K. Jordan, M. Shinn, and T. Siggins. Jefferson lab IR demo FEL photocathode quantum efficiency scanner. *Nuclear Instruments and Methods in Physics Research Section A: Accelerators, Spectrometers, Detectors and Associated Equipment*, 475(1):554–558, 2001.

[29] P.A. Corlett and J.H.P. Rogers. ERLP quantum efficiency scanner. In *Proceedings of EPAC*, 2006.

[30] D. Sertore, P. Michelato, L. Monaco, and C. Pagani. A study for the characterization of high QE photocathodes. In *Particle Accelerator Conference, 2007. PAC. IEEE*, pages 2760 –2762, june 2007.

[31] L. Cultrera, I. Bazarov, A. Bartnik, B. Dunham, S. Karkare, R. Merluzzi, and M. Nichols. Thermal emittance and response time of a cesium antimonide photocathode. *Applied Physics Letters*, 99(15):152110, 2011.

[32] F. Zhou, A. Brachmann, F-J. Decker, P. Emma, S. Gilevich, R. Iverson, P. Stefan, and J. Turner. High-brightness electron beam evolution following laser-based cleaning of a photocathode. *Phys. Rev. ST Accel. Beams*, 15:090703, Sep 2012.

[33] S. Roychowdhury. *High Brightness Electron And Photon Beams*. PhD thesis, Duke University, 2006.

[34] B. C. Riddick, E. J. Montgomery, R. B. Fiorito, H. D. Zhang, A. G. Shkvarunets, Z. Pan, and S. A. Khan. Photocathode quantum efficiency mapping at high resolution using a digital micromirror device. *Phys. Rev. ST Accel. Beams*, 16:062802, Jun 2013.

[35] H. D. Zhang, R. B. Fiorito, A. G. Shkvarunets, R. A. Kishek, and C. P. Welsch. Beam halo imaging with a digital optical mask. *Phys. Rev. ST Accel. Beams*, 15:072803, Jul 2012.

[36] J. T. Fong, T. W. Winter, and S. J. Jacobs. Advances in DMD-based UV application reliability below 320nm. In *Society of Photo-Optical Instrumentation*

Engineers (SPIE) Conference Series, volume 7637 of *Society of Photo-Optical Instrumentation Engineers (SPIE) Conference Series*, March 2010.

[37] M Skottke-Klein, A Böttcher, R Imbeck, S Kennou, A Morgante, and G Ertl. Preparation and characterization of thin CsAu films. *Thin Solid Films*, 203(1):131–145, 1991.

[38] S.A. Khan, E.J. Montgomery, B.C. Riddick, and P. O'Shea. Fabrication and characterization of cesium-based photocathodes for free electron lasers. *Journal of Vacuum Science & Technology B: Microelectronics and Nanometer Structures*, 30(3):031207, 2012.

[39] W. E. Spicer, A. H. Sommer, and J. G. White. Studies of the semiconducting properties of the compound CsAu. *Phys. Rev.*, 115:57–62, Jul 1959.

[40] W. E. Spicer. Photoemission and band structure of the semiconducting compound CsAu. *Phys. Rev.*, 125:1297–1299, Feb 1962.

[41] R. A. Kishek. Charged Particle Dynamics class at the University of Maryland, 2011.